University of Crete
School of Science and Engineering
Department of Physics
Supervisor: Dr. Paraskevas Tzallas

Master Thesis

High reflectivity XUV focusing system using toroidal mirrors and a hexapod robot device

Student:	Panagiotis Konstantakis
Studies:	Photonics & Nanoelectronics
Semester:	4
Student ID:	668

Heraklion, 13/7/21

Table of Contents

List of Abbreviations and Symbols

XUV	Extreme ultra violet
EUV	Extreme ultra violet
a.u.	Arbitary units

Abstract

Advancements in laser science and technology enabled the development of ultrashort laser pulses and the production of XUV isolated and train of pulses. These scientific and technological breakthroughs lead to the investigation of ultrafast phenomena and strong-field physics, including non-linear phenomena between laser pulses and atoms. Multiphoton ionization as a non-linear phenomenon requires high laser pulse intensity to be observed. Short-pulse duration, coupled with high energy per pulse (μj order) and an appropriate focusing element is the perfect combination for achieving high intensities (above $10^{12} W/cm^2$) for multiphoton ionization, which is essential for pump-probe studies on the XUV regime. However, focusing XUV radiation is not trivial, due to the radiation's high absorption in commonly used optical materials. This leads to totally avoiding refractive optics, and using reflective optics to steer and focus an XUV beam. Two of the most common approaches employed on this matter are spherical gold or multilayer mirrors in near-normal incidence. Nonetheless, limitations arise due to the angle of the radiation that strikes the spherical mirror (to avoid spherical aberrations, coma and astigmatism) and the relative low reflectivity of multilayer mirrors for broadband range radiation. Another solution to this problem is the choice of a pair of gold-coated toroidal mirrors, used in near grazing incidence which can focus the XUV beam and minimize the aberrations. This thesis contains the procedure of the development and characterization of an experimental setup that uses a pair of toroidal mirrors mounted on a hexapod robot device to focus a IR beam and a XUV beam. Our goal was to find the optimum, experimental parameters for achieving the minimum spot size (with minimum aberrations) for an IR beam. It also contains simulations of the setup using Zemax, combining methods of ray tracing and physical optics.

1 Introduction

Isolated attosecond pulses or attosecond pulse trains can be produced by bursts of coherent EUV radiation generated by means of high harmonic generation [1,2]. The photon energies of EUV radiation range approximately between $10\,eV$ and $124\,eV$ where many atomic resonances can be traced as shown in figure 1a, 1b. Due to the strong absorption of the EUV in the matter, refractive optics are not appropriate to be used in this range of radiation. In figure 1c is shown the attenuation levels for some common materials used in optical lenses. There have been some efforts to develop refractive optics for EUV radiation, using rare gasses to focus the beam produced by HHG [3], but this method is not practical in a typical experimental setup (control of the backing pressure of the jet and the gas density gradient, use of specific gas, etc). Another options are diffractive optics such as Fresnel zone plate [4] and reflective optics like metal coated or multilayer mirrors of various shapes (spherical, toroidal, ellipsoid, etc) [5]. Fresnel zone plates typically suffer from low reflectivity and chromatic aberrations that limit the minimum achievable spot size [6,7]. Some of the most common solutions are the implementation of a reflective spherical mirror [8,9] (metal or multilayer), or gold coated toroidal mirrors, in pairs [10].

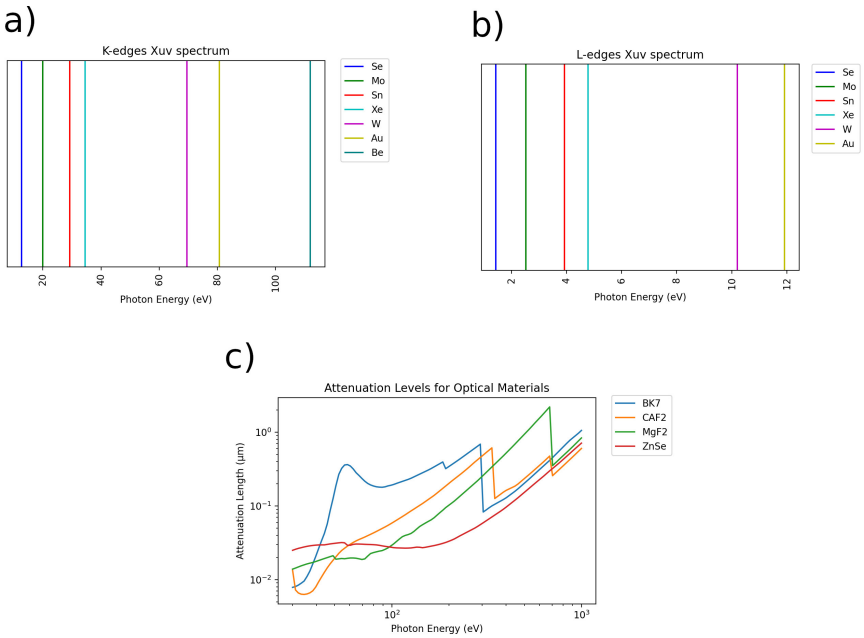

***Figure 1**: **a)** K-edge absorption lines for some common chemical elements for photon energies between 10 and 80 eV [11]. **b)** L-edge absorption lines for photon energies between 1 and 11 eV [11]. **c)** Attenuation length for materials that are used for manufacturing optical lenses for UV and IR applications [12], [13].*

1.1 Spherical mirrors for XUV focusing

Spherical-shaped mirrors are one of the most broadly used types of optics that can handle and focus the XUV radiation. The two big categories of spherical mirrors are metal (Au, Silver, etc) or multilayer. Both types are prone to monochromatic aberrations, which can be described based on third-order aberration theory. These kinds of aberrations are called Gauss-Seidel aberrations and spherical mirrors typically can suffer from spherical aberration, coma, astigmatism.

1.1.1 Third Order aberration theory for spherical mirrors

First, we will calculate the Gauss-Seidel aberrations for a spherical mirror based on the third-order aberration theory [14]. In figure 2 can be seen, a spherical mirror with rays starting from the object and traced to the spherical mirror surface. After reflection from the spherical mirror, the rays are forced to converge to the paraxial focus, regardless if they would physically end up there.

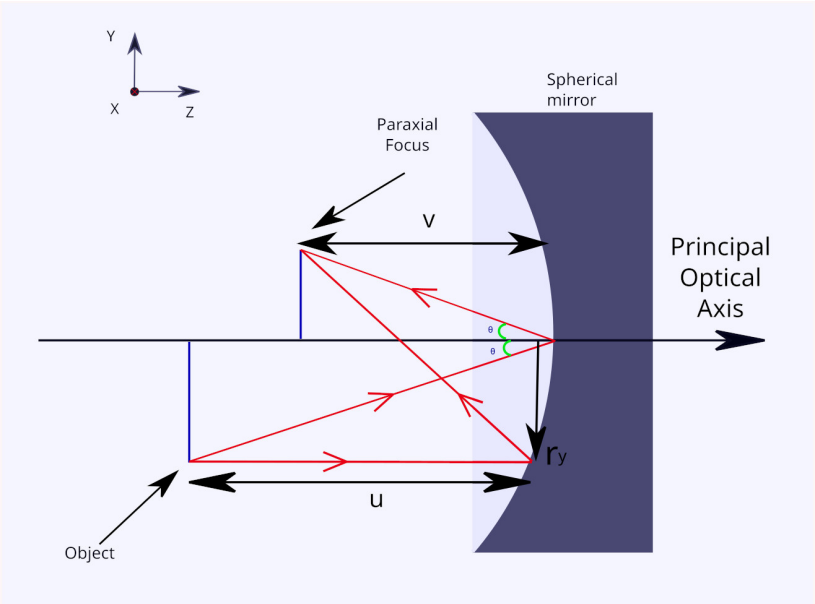

***Figure 2**: Ray trace for a spherical mirror, where the rays are forced to converge to the paraxial focus after the reflection from the last spherical mirror surface. The distance of the object is u from the spherical mirror surface and the distance of the paraxial focus image is v.*

The position vectors of the rays in the object, mirror surface and image are equal to:

Object vector: $\vec{p}_{Obj} = -u\theta\,\vec{j} - u\,\vec{k}$.

Surface vector: $\vec{p}_{Ms} = r_X\,\vec{i} + r_Y\,\vec{j} + \left[\left(r^2/2R\right) + \left(r^4/8R^3\right)\right]\vec{k}$.

Image vector: $\vec{p}_{Ima} = -v\theta\,\vec{j} + v\,\vec{k}$.

The $-u$ is the object distance, v is the image distance, r_X is the distance of the projection of rays on the spherical mirror surface to the *x axis*, the same holds for r_Y but for the *y axis*. The r is equal to $r=\sqrt{r_X^2+r_Y^2}$ and R is the radius of the spherical mirror.

The total path that rays follow from object to the paraxial focus is equal to:

$$\Phi=\sqrt{\left(\vec{p}_{XMs}-\vec{p}_{XObj}\right)^2+\left(\vec{p}_{YMs}-\vec{p}_{YObj}\right)^2+\left(\vec{p}_{XMs}-\vec{p}_{XObj}\right)^2}$$
$$+\sqrt{\left(\vec{p}_{XIma}-\vec{p}_{XMs}\right)^2+\left(\vec{p}_{YMs}-\vec{p}_{YObj}\right)^2+\left(\vec{p}_{XIma}-\vec{p}_{XMs}\right)^2}\Rightarrow$$

which after some calculations Φ is equal to:

$$\Phi=\sqrt{2r_y u\theta+(u\theta)^2+u^2+(1+u/R)r^2+\left(1/4R^2+u/4R^3\right)r^4+r^6/8R^4+r^8/64R^6}$$
$$+\sqrt{2r_y v\theta+(v\theta)^2+v^2+(1-v/R)r^2+\left(1/4R^2-v/4R^3\right)r^4+r^6/8R^4+r^8/64R^6}$$

Then we drop the r^6, r^8 terms as part of the third-order aberration theory, and we keep only r^4 terms and below:

$$\Phi\approx u\sqrt{1+2r_y\theta/u+\theta^2+\left(1/u^2+1/uR\right)r^2+\left(1/4u^2R^2+1/4uR^3\right)r^4}$$
$$+v\sqrt{1+2r_y\theta/v+\theta^2+\left(1/v^2-1/vR\right)r^2+\left(1/4v^2R^2-v/4vR^3\right)r^4}$$

The r^2, u^2, v^2 are the paraxial terms which, we will not consider in order to study the aberrations. We will concentrate on the rest of the terms by calculating the square roots by applying the binomial approximation ($\sqrt{1+x}\approx 1+x/2$) and combining the results with the thin lens equation $1/u-1/v=-2/R$, we get:

$\Phi_{SA}=-1/(4R)(1/u+1/R)^2 r^4$ (Spherical Aberration),
$\Phi_{CO}=-1/R(1/u+1/R)r^2 r_y\theta$ (Coma),
$\Phi_{AS}=-(1/R)r_y^2\theta^2$ (Astigmatism),
$\Phi_{FC}=0$ (Field Curvature).

These formulas, practically mean that spherical aberration increases as the r^4 term increases, or the rays hit further away from the center of the spherical mirror. Both coma and astigmatism increase by increasing the incidence angle θ of the rays with the surface of the spherical mirror. Examples of these aberrations can be seen in figure 3. All these aberrations can reduce the intensity of the focused beam, increase the duration of an attosecond pulse, or even create double pulse front. Such alterations can affect the resolution of pump-probe experiments, cause unwanted double excitations etc [15].

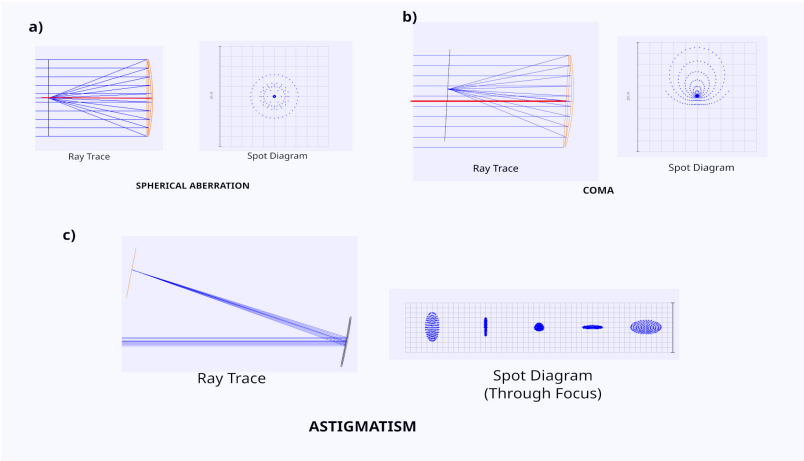

***Figure 3**: Ray trace and spot diagrams on the focus of a spherical mirror. **a)** Spherical aberration pattern where the rays' spots, make circles of different sizes around the central spot. **b)** Coma aberration pattern where the rays' spots have a comet-like shape. **c)** Astigmatism pattern where tangential and sagittal foci are in different positions around the focus area.*

1.1.2 Reflectivity and different types of spherical mirrors

The reflectivity of a spherical mirror (or any reflective optical element) depends on two important factors. The first one is the angle of incidence (the angle between the rays of light and the line perpendicular to the surface at the point of contact).
The reflectivity of the surface which is surrounded by air is equal to:

$R_S = \left|\cos\varphi - \sqrt{n^2 - \sin^2\varphi}\right|^2 / \left|\cos\varphi + \sqrt{n^2 - \sin^2\varphi}\right|^2$ (perpendicular to the surface polarization)
$R_p = \left|n^2\cos\varphi - \sqrt{n^2 - \sin^2\varphi}\right|^2 / \left|n^2\cos\varphi + \sqrt{n^2 - \sin^2\varphi}\right|^2$ (parallel to the surface polarization)

The reflectivity plot for a thin film of Au can be seen in figure 4, from which we can conclude that as the incidence angle approaches $90°$ the reflectivity increases. This is the basic principle for grazing incidence optics. Usually, the coating can be as simple as a thin film of Au which can achieve $10\%-20\%$ reflectivity in near-normal incidence for photon energies of $10\,eV$ [16]. More complicated coatings can be used in order to achieve higher reflectivities for certain photon energies. Periodic multilayers can be used where layers of combinations of 2 or 3 materials are deposited on a type of glass substrate (BK7, SiO_2 etc), and they offer higher reflectivities $20\%-40\%$ for photon energies between $31\,eV-34\,eV$ [17]. Aperiodic multilayers can also be used, and they offer lower reflectivities $15\%-20\%$, for a broadband radiation of $35\,eV-50\,eV$ appropriate for handling XUV pulses [18]. Examples of such multilayer coatings can be found in figure 5.

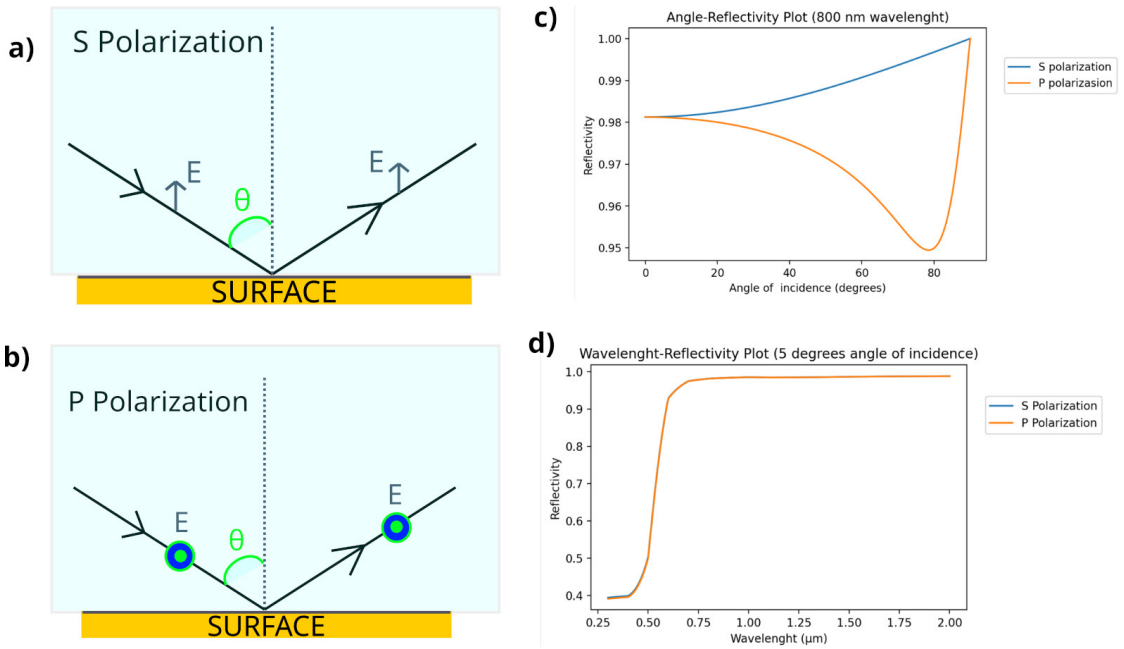

Figure 4: *Angle of incidence θ for a ray with* ***a)*** *S polarization* ***b)*** *P polarization. Reflectivity of a thin film of Au based on experimental measurements [19], while changing* ***c)*** *angle for 800 nm wavelength* ***d)*** *wavelength for a five degrees incidence angle.*

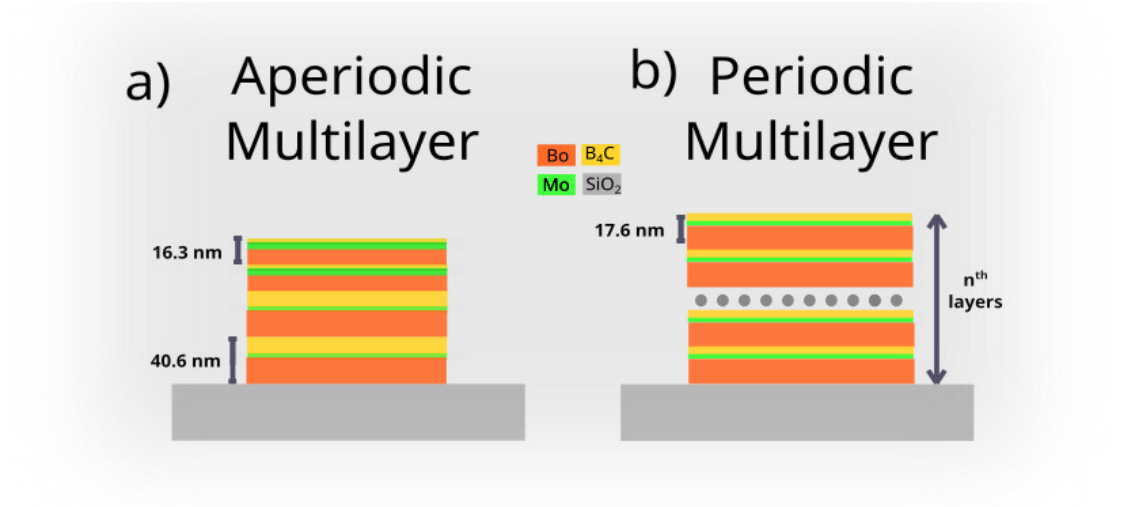

Figure 5: *Examples of* ***a)*** *aperiodic multilayer mirror where different stacks of layers are interchanged [18]* ***b)*** *periodic multilayer mirrors [17], made from repeating layers of 3 different materials, Bo, Mo, B_4C.*

1.1 Toroidal mirrors and grazing incidence optics

Spherical mirrors have a couple of limitations when used in an experimental setup involving EUV radiation. First, big aperture beams should be avoided in order to minimize spherical aberration. Second, the laser beam should be reflected in nearly-normal incidence angle in order to avoid coma and astigmatism. A combination of nearly-nor-

mal incidence angles, lead to low reflectivities even when used in pair with multilayer coatings for broadband radiation. But how, do you achieve high reflectivities for a broadband radiation while avoiding the different types of monochromatic aberrations? The answer is pairs of optics in combination with grazing incidence angle to achieve very high intensities and fix optical aberrations [20].

1.1.1 Wolter optics and Abbe condition

Generally, the refractive index can be expressed as $n=1-\delta-i\beta$ where δ is the phase change and β expresses the absorption. Both δ, β are functions of photon's wavelenght and the radiation can be totally reflected for grazing angles lower than $\cos(\alpha_t)=1-\delta$ [21]. In reality, there is still some absorption as the β does not vanish and there are specific absorption lines for each chemical element. Every optical system, as complex as It is, can always be described by only two planes which are called principal planes where the magnification is unity [14], as can be seen in figure 6a. An imaging system free from aberrations can be described by the Abbe condition that can be expressed simply as $d/sin\theta=f$ where f is the focal length, d is the distance from the principal optical axis and θ is the ray's angle with the optical axis as can be seen in figure 6b. In simple terms, Abbe condition means that the principal image plane should be a spherical surface, in order for paraxial rays to have the same distance from the focus, as can be seen in figure 6c. For a single optical surface, the principal image plane is the same as the optical surface. For example, a spherical optical surface can meet this condition as shown in figure 7 but the same is not true for an ellipsoidal surface [21].

The solution is to use two-mirror systems [21, 22] of various types such as elliptical, hyperbolic, parabolic mirrors in order to minimize aberrations and losses from reflections. Those types of systems are known as Wolter optics configurations and an example of such configuration can be seen in figure. In practice, in the place of the ellipsoidal mirrors we can use pairs of toroidal mirrors, which are easier and cheaper to manufacture [5]. The surface of a toroidal mirror is equal to the surface of the outer part of a torus, which can be approximated by an ellipsoid like in figures 7a, 7b [23]. The toroidal mirrors have two different radius for tangential (the plane which includes both optical axis and the normal to the mirror surface) and the sagittal plane (normal to tangential plane, and It also includes the optical axis). Each radius can be set independently in order to minimize astigmatism and the focal length for each plane is $f_T=R_T\,sin\theta/2$ (tangential) and $f_S=R_S/2\,sin\theta$ (sagittal). For the previous formulas, R_T, R_S are the radius for tangential and sagittal planes and θ is the grazing angle.

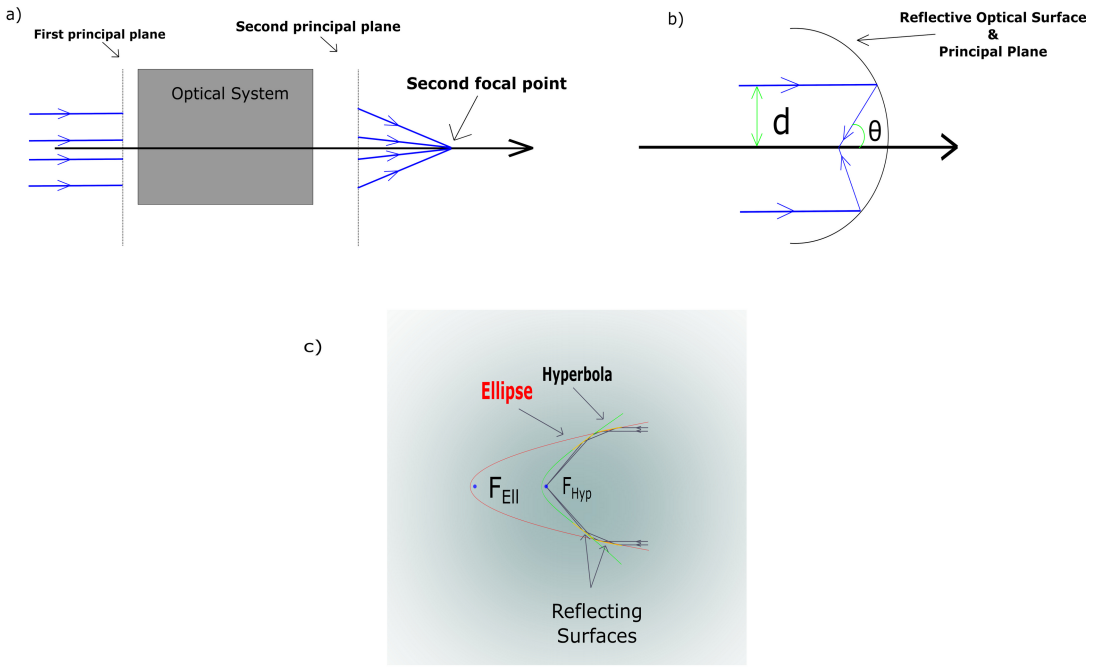

Figure 6: a) *Principal plane for an arbitrary system where the paraxial rays are focused on the second focal point.* ***b)*** *Example of a reflective optical surface which coincides with the principal plane.* ***c)*** *Example of a Wolter optics configuration with an ellipsoid and a hyperboloid mirror.*

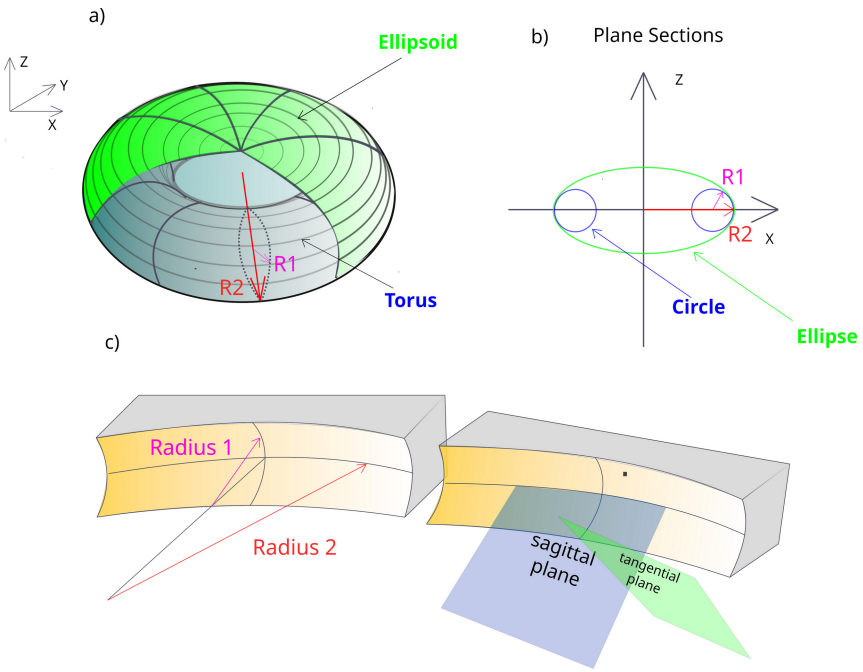

Figure 7: a) *A graphic example of a torus inside an ellipsoid, which indicates that the outer part of the torus surface can be a good local approximation for the ellipsoid.* ***b)*** *A plane section of the torus and the ellipsoid of the figure a.* ***c)*** *A pair of toroidal mirrors where the tangential and sagittal plane and their radii are shown.*

2 Simulations of the experimental setup using Zemax

In this chapter, we will discuss in detail the procedure that we followed in order to simulate the optical system that we used in the laboratory to focus the IR pulses of $800\,nm$ central wavelength and $24\,fs$ duration [24]. The optical system that was used, is a pair of gold-coated toroidal mirrors manufactured by THALES SESO. For the analysis of the system, they were used both ray trace and physical optics propagation modules of the Zemax. Our goal was to analyze the aberrations, due to misalignment and the tilts of the toroidal mirrors.

2.1 Basics of Zemax ray tracing and physical optics propagation modules

The basic working principle of the Zemax is based on optical surfaces. Zemax can be used with two modes, the first one is the sequential mode and the second one is the non-sequential mode. In the sequential mode, the rays trace strictly from surface 1, to surface 2, to surface nth in order to describe the optical system. In the case of the non-sequential mode rays follow the laws of reflection and refraction and can trace to any surface, or three-dimensional objects without any particular order. So, how do we design an optical system in Zemax? First, we choose an appropriate surface for each optical element. Then, we add an aperture for each surface and choose the material after each surface. Finally, we add a coating for each optical surface. Materials and coatings have certain optical characteristics based on the refractive index for each wavelength. A graphic example of the procedure can be seen in figure. In our case, our optical system contains 5 surfaces, as can be seen in figure 8a.

The rays start from the image plane and follow their path through the object stop (controls the illumination of the object). In the figure we can see, the chief ray (the ray that passes through the center of object stop) and the marginal ray (the ray that passes from the sides of object stop). The chief ray has a $5°$ grazing angle with the first toroidal mirror surface. The object aperture has a $6\,mm$ diameter, just enough for the rays to illuminate the surface of the first toroidal mirror. The toroidal mirrors are made from a biconic toroidal surface with a rectangular aperture ($70\,mm \times 10\,mm$) and with radii $22.54\,mm$ (sagittal, Radius 1 figure 7c), $16140\,mm$ (tangential Radius 2 figure 7 c). For the second toroidal mirror the aperture is the same as the first one, and with radii $280\,mm$ (sagittal, Radius 1 figure 7c), $37000\,mm$ (tangential, Radius 2 figure 7 c). Underneath the toroidal surface is used a material with the name MIRROR, which has reflectance $R=1$. The coating on the surface which is applied is a $170\,nm$ thin film of Au, in which the refractive index is obtained from [19] for a wavelength $\lambda_{IR}=800\,nm$. The refractive index for the XUV radiation was calculated from the scattering factor of Au for the 13th harmonic $\lambda_{XUV\,(13^{th})}=61.54\,nm$ and the 25th harmonic $\lambda_{XUV\,(25^{th})}=32\,nm$, of the IR field produced by high harmonic generation. Also the reflectivities of Au for different angles of incidence and for the 13th and 25th harmonics are shown in figure 9. The refractive index is calculated from the scattering factors and is given from the formula, $n=1-n_\alpha r_e \lambda^2/[(2\pi)(f_1^0-if_2^0)]$ [11] where the $n_a \approx 5.76\cdot 10^{22}\,atoms\cdot cm^{-3}$ is the atomic number density, the $r_e \approx 2.82\cdot 10^{-13}\,cm$ is the classical electron radius, the $f_1^0=5.25\ \ (e\cdot atom^{-1})$ is the real part of the atomic scat-

tering factor and $f_2^0 = 15.74\ \left(e \cdot atom^{-1}\right)$ [25] is the imaginary part of the atomic scattering factor. The XUV refractive index is then equal to $n_{XUV\,(13^{th})} \approx 0.49 - 1.54\,i$. The refractive index of Au for the XUV radiation was also calculated for the 25th harmonic $\lambda_{XUV\,(25^{th})} = 32\,nm$ and is equal to $n_{XUV\,(25^{th})} \approx 0.45 - 0.29\,i$.

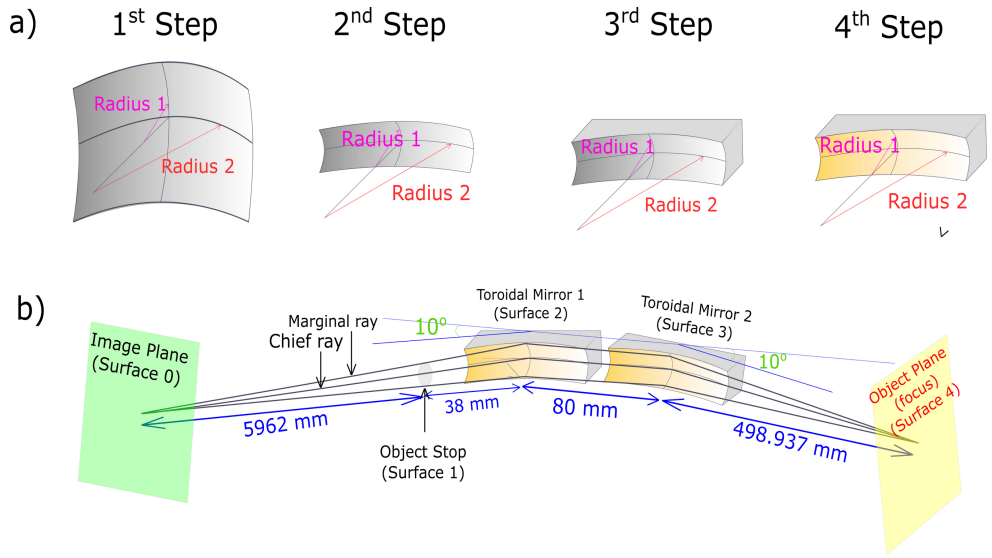

Figure 8: a) *Steps to follow in order to design an optical element. First, we choose a biconic toroidal surface (step 1), with a rectangular aperture (step 2). Then we add a MIRROR type material (100% reflectivity) underneath the surface (step 3). Finally, we add a gold coating with a thin BK7 substrate.* ***b)*** *A graphic visualization of the experimental setup's ray trace.*

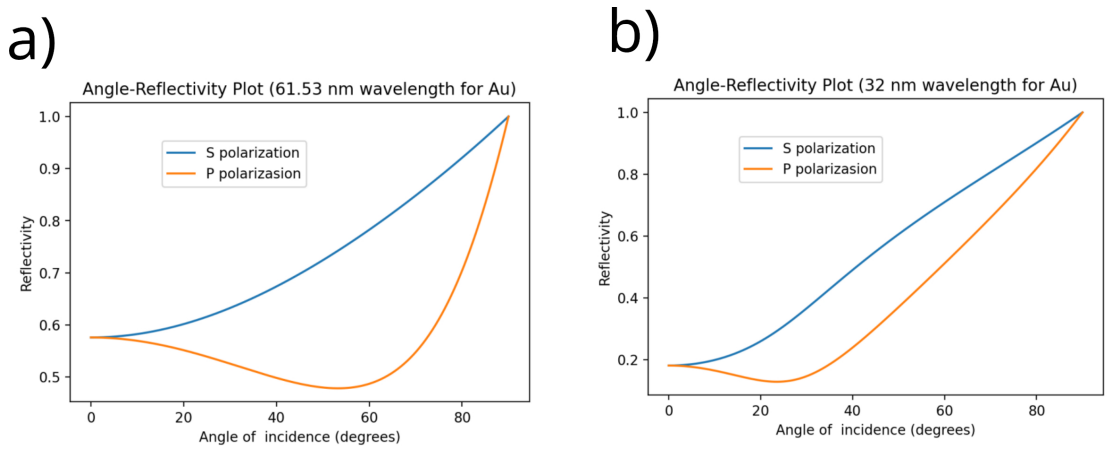

Figure 9*: Reflectivity of Au for different angles of incidence for a wavelength* ***a)*** *61.53 nm (13th harmonic).* ***b)*** *32 nm (25th harmonic). For the 13th harmonic, the reflectivity for Au is overestimated due to uncertainties in scattering factors values taken from reference [25].*

2.1.1 Ray tracing versus physical optics propagation

Ray tracing calculations are based on the propagation of light in straight lines which are normal to the surface of the wavefront (constant phase surface) like in figure 10a. The rays are always propagating in a straight line which limits their application during focusing (they cannot predict with accuracy the intensity profile of the beam near the focus like in figure 10b). Also, for a collimated beam (with minimum divergence, but still expanding due to diffraction), the rays that describe the propagation of the beam are parallel between them and won't describe the slow expansion, like in figure 10b. However, the distribution of the rays can express the beam profile with good accuracy in the far-field [26]. So, where does the link between wave optics and ray optics comes from? First, let $U(\vec{r})=a(\vec{r})\exp[-jk_o S(\vec{r})]$, be the complex amplitude of a monochromatic wave inside a medium with refractive index n. The product of $-k_o S(\vec{r})$ is equal to the phase of the wave, which for a surface where $S(\vec{r})=constant$ is by definition a wavefront. The complex amplitude is then substituted to the Helmholtz equation $\nabla U^2+k^2U=0$ which leads to two equations $k_o^2[n^2-|\nabla S|^2]\alpha+\nabla^2\alpha=0$ (real part) and $-k_o(2\nabla S\cdot\nabla\alpha+\alpha\nabla^2 S)=0$ (imaginary part). From the imaginary part we get the equation $|\nabla S|^2=n^2+(\lambda_o/(2\pi))^2(\nabla^2\alpha/\alpha)$ which is approximately equal to $|\nabla S|^2\approx n^2$, if we neglect the second term ($(\lambda_o/(2\pi))^2(\nabla^2\alpha/\alpha)\ll 1$) [27]. This equation is called Eikonal equation from which can be derived the Fermat principle [28]. The Fermat principle, is essentially the basis for ray optics.

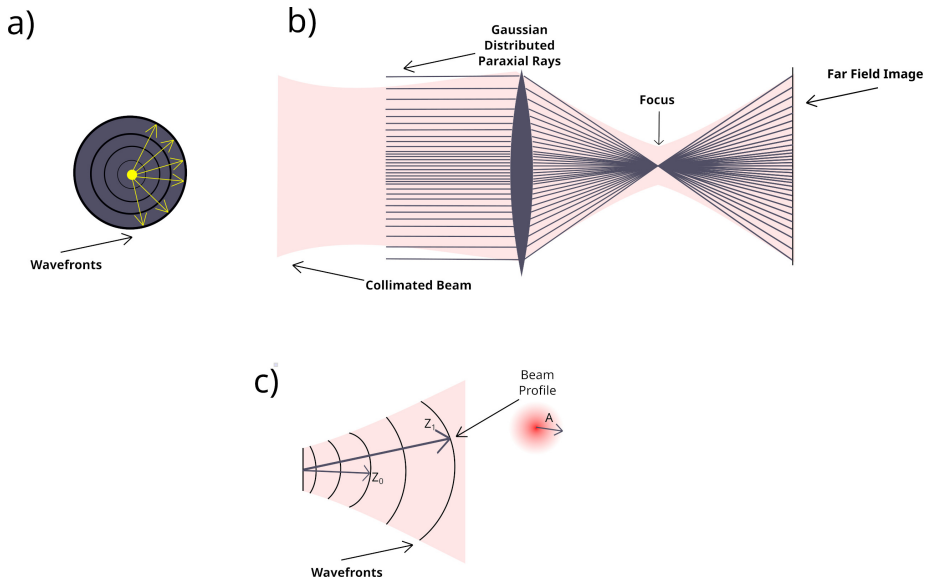

Figure 10: a) *Depiction of rays, and wavefronts produced from a point source of light. The rays are always normal to the surface of the wavefronts.* ***b)*** *Collimated Gaussian beam, described by a set of rays with a Gaussian distribution, focused from a thin lens. The rays converge to a point instead of forming an Gaussian distribution at the focus, as one would expect from wave optics.* ***c)*** *Graphic example of a beam wavefront as It expands due to diffraction. As Z_0 increases compared to Z_1 and the Z_{eff} becomes smaller. Also A the radial beam size gets bigger and the beam is considered to be in the far-field (Fresnel number increases, comparing between Z_0 and Z_1).*

On the other side, physical optics propagation works by calculating the electric field of the beam, based on one parameter called Fresnel number. Fresnel number can be simply expressed as $F_n = A^2/(\lambda Z_{eff})$ where A is the radial size of the beam and $Z_{eff} = (Z_1 - Z_0) Z_0 / Z_1$, where Z_0 is the radius of a wavefront for a reference point and Z_1 is the radius of the wavefront in the spot of the observation point like in figure 10c. As a rule of thumb, if $1 \leqslant F_n \leqslant \infty$ then the beam is considered as being in the near field compared to the reference point. On the other hand, if $0 \leqslant F_n \leqslant 1$ is considered as being in the far-field [29]. Based on the Fresnel number calculations, Zemax chooses the appropriate algorithms to calculate the propagation of the beam. For a large Fresnel number the angular spectrum propagation method is used to calculate the beam parameters as It propagates through the optical system. For smaller Fresnel number, an algorithm based on Fresnel diffraction is used.

2.1.2 Fresnel diffraction and angular spectrum propagation

For the basis of the angular spectrum propagation we start from a plane wave like in figure 11a. The equation for the plane wave is $e^{i\vec{k}\cdot\hat{z}} = e^{ik_z \cdot z}$ where $\vec{k}$ is wave vector which is normal to the wave fronts and z the local axis. The direction of k is indicated by direction cosines α, β, γ which satisfy the relationship $\alpha^2 + \beta^2 + \gamma^2 = 1$. The value of the wave number is given by the formula $k^2 = k_x^2 + k_y^2 + k_z^2 \Rightarrow k_z = k\sqrt{1 - (k_x/k)^2 + (k_y/k)^2} \Rightarrow k_z = k\sqrt{1 - \alpha^2 - \beta^2}$. So the equation for the plane wave becomes $e^{ik_z \cdot z} = e^{ik \cdot z\sqrt{1-\alpha^2-\beta^2}} \approx e^{ikz} e^{-ikz(\alpha^2+\beta^2)/2} \approx e^{-ikz(\alpha^2+\beta^2)/2}$ which simplifies by considering that $\vec{k}$ vector has a small angle with z axis and by dropping the e^{ikz} term. The final result is the transfer function of a plane wave inside homogeneous media. Now the transfer function can be rewritten using the spatial frequency variables ξ, η which are connected with the direction cosines through the relationships $\alpha = \lambda\xi$ and $\beta = \lambda\eta$ as $e^{-ikz(\alpha^2+\beta^2)/2} = e^{-ikz\lambda^2((\alpha/\lambda)^2+(\beta/2)^2)/2} = e^{-i\pi\lambda z(\xi^2+\eta^2)} = e^{-i\pi\lambda z\rho^2}$. The frequency variables, are introduced through the Fourier transform of the electric field, of the beam $E(x,y) = \int_{-\infty}^{\infty}\int_{-\infty}^{\infty} G(\xi,\eta) e^{i2\pi(\chi\xi+y\eta)} d\xi d\eta$. So the calculation of the electric field for a displacement Δz can be calculated by first applying the transfer function to G(ξ,η) and then using reverse Fourier transform to calculate the electric field after the displacement. This can be summarized in one line as $PTP(E, \Delta z) = FF^{-1}[T(\Delta z) G(\xi,\eta)]$, where PTP is the plane to plane operator, FF^{-1} is the reverse Fourier transform and $T(\Delta z)$ the transfer function [29,26].

For the Fresnel approximation we begin by defining two parallel coordinate systems, XYZ and $X'Y'Z$ with common Z axis and distance z between them. We start from the Huyghens-Fresnel principle $U(P_0) = \frac{1}{i\lambda}\int\int_{\Sigma} U(P_1)\exp(ikr_{01})\cos\theta / r_{01} ds$ in order to calculate the wavefield across $X'Y'Z$ plane. P_0 is a point of the $X'Y'$ plane, P_1 a point of XY plane, $\cos\theta = z/r_{01}$ and $r_{01} = \sqrt{z^2 + (x'-x)^2 + (y'-y)^2}$ the distance between P_0 and P_1 like in figure 11b. The integral can be expressed based on x, y and x', y' coordinates as $U(x', y') = \frac{z}{i\lambda}\int\int_{\Sigma} U(x,y)\exp(ikr_{01})/r_{01}^2 dxdy$.

The previous expression can be further simplified by applying binomial expansion as $r_{01}=z\sqrt{1+[(x'-x)/z]^2+[(y'-y)/z]^2}\approx z[1+(1/2)[(x'-x)/2]^2+(1/2)[(y'-y)/2]^2]$. This approximation results in an expression for the wavefield, that is equal to $E(x',y')=\frac{e^{ikz}}{i\lambda z}e^{ikz(x'^2+y'^2)/(2z)}\iint_{-\infty}^{\infty}E(x,y)e^{ik(x^2+y^2)/(2z)}e^{-i2\pi(xx'+yy')/(\lambda z)}dx\,dy$ and It used by the algorithm to calculate the electric field [26, 30].

a) b)

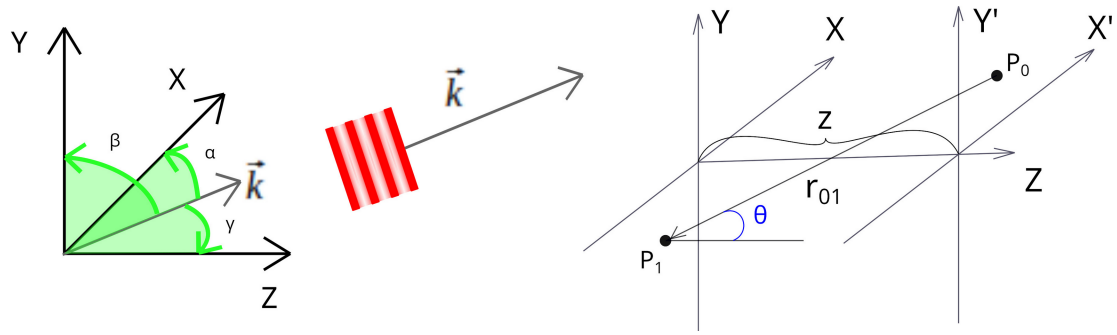

Figure 11: α) *Plane wave with k vector normal to the wavefronts indicating the direction of propagation with, direction cosines α, β, γ for x, y, z axis respectively.* ***b)*** *Two parallel coordinate systems XYZ and X'Y'Z with common Z axis and P_0, P_1 points of X'Y', and XY planes respectively.*

2.2 IR and XUV beam parameters

Zemax takes as input the beam size at the starting surface of the beam propagation (which is chosen by the user) and the half angle divergence at the far field [26]. In the simulation was used a Gaussian beam and the parameters were determined based on the experimental setup that was used in the laboratory.

2.2.1 Experimental setup and beam parameters determination

In order to to calculate the initial conditions of the beam, we need to examine a simplified view of the experimental setup used inside the laboratory. The experimental setup can be seen in figure 12a. The laser pulse, follows a path from a silver flat mirror, to a gold spherical mirror of $f_{SM}\approx 9m$ focal length, with a very small angle of incidence (around $3°$). In the region of focus of the spherical mirror, there is a gas-jet target from which the XUV pulse is produced through high harmonic generation. The input for the simulations of the beam with Zemax depends on the size of the beam on the spherical mirror, which can be controlled via an iris before the spherical mirror. Before continuing let us make a small introduction to the Gaussian beam. The spatial intensity of a Gaussian beam is given from the relationship $I(r,z)=I_0(w_0/w(z))^2\exp(-2r^2/w(z)^2)$, where $w(z)=w_0\sqrt{1+(z/z_r)^2}$ is called beam radius, z is the distance from the focus of the beam, I_0 is the maximum intensity at the center of the beam at the focus, r is the radial distance from the center of the

beam [26] as can be seen in figure 12b. The starting surface of the beam inside the simulation is located at distance $d_1+d_2=5800\,mm$ from the spherical mirror as can be seen in figure 11a, with a total distance $d_1+d_2+d_3+d_4=6000\,mm$ (total distance, until the beam reaches the first toroidal mirror). For the IR beam a beam diameter (or full width at $1/e^2$, or $2w(z)$) of $D_{SM(IR)}=2w_{SM(IR)}$ was estimated based on the experimental conditions of the next chapter. The divergence θ of the beam (see figure 12b) on the far field is approximately $\theta_{IR}\approx w_{SM(IR)}/f_{SM}$, which results in a diameter on the starting surface $D_{SS(IR)}\approx 2\theta_{IR}(d_1+d_2)$. With a similar thought process for the XUV beam we calculated the parameters, which now depend on the fundamental IR beam which has different characteristics compared to the previous one (IR beam) in order to produce the XUV beam through HHG. Generally, the divergence of the XUV beam depends of different factors such as the wavelength and the waist of the harmonic, the trajectory coefficients, etc [31]. For the XUV beam, the resulting divergence is $\theta_{IR}\approx w_{SM(IR)}/f_{SM}$ and $\theta_{XUV}\approx\theta_{IR}/\sqrt{(q_{eff})}$, where q_{eff} is the effective nonlinearity coefficient [32]. So, the diameter of the XUV beam at the starting surface is $D_{SS(XUV)}\approx 2\theta_{XUV}(d_1+d_2)$. The polarization of the beams, is parallel to the surface of the mirrors (p polarization). In the table 1 are shown the most important parameters, for the simulations.

Table 1: Basic parameters for the simulations of the experiment

Without HHG				
λ (nm)	**2θ (mrad)**	**D_{SM} (mm)**	**D_{SS} (mm)**	**q_{eff}**
800	1.11	10	6.44	-
With HHG				
λ (nm)	**2θ (mrad)**	**D_{SM} (mm)**	**D_{SS} (mm)**	**q_{eff}**
800	2.78	25	16.11	-
61.54	1.39	-	8.06	4
32	1.31	-	7.59	4.5

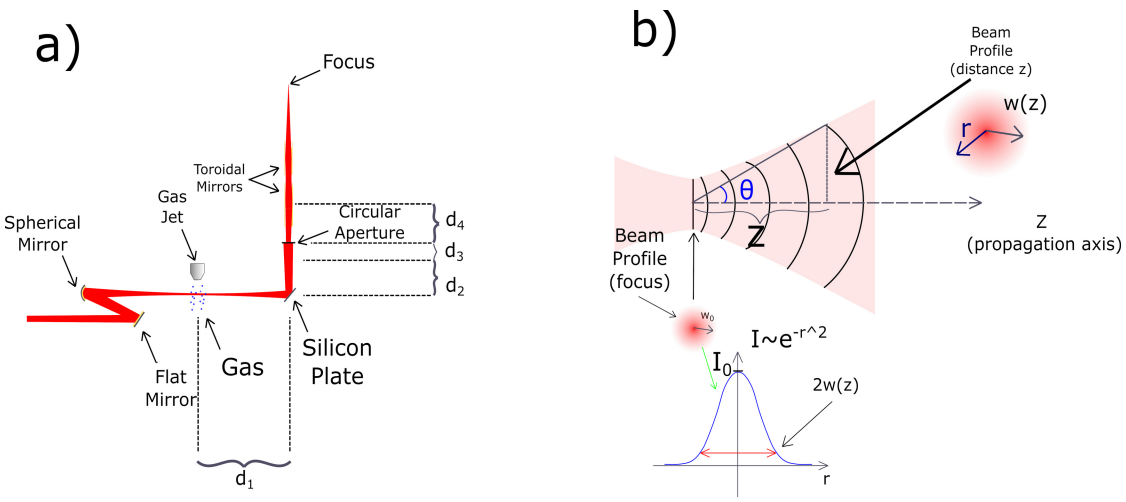

Figure 12: a) *Simplified view of the experimental setup, where the IR beam follows a path from the flat mirror to spherical mirror which focuses the beam on the gas jet target in order to achieve HHG and produce an XUV beam. Then a silicon plate steers the beam to a circular aperture after which is microfocused from the pair of toroidal mirrors. d_1 is the distance from the focus of the beam to the silicon plate, d_2 from the silicon plate to the surface where the simulation begins, d_3 from the starting surface of the simulation to the circular aperture and d_4 from the circular aperture to the first toroidal mirror.* ***b)*** *Depiction of the basic parameters, of a Gaussian beam. Here is shown, the divergence θ, the intensity profile on the focus of the beam with maximum intensity I_0, as well as the profile of the beam in a distance z.*

2.3 Simulation with Zemax results and analysis

Before proceeding with the results of the simulations, let us make a brief introduction in order to describe the movement of the toroidal mirrors. The toroidal mirrors are packed inside a metal housing, like in figure 13c. This is very important because the optical system is very sensitive and the angle and the distance between the toroidal mirrors should be kept intact. The toroidal mirrors movement is controlled with the help of a hexapod robot device (further details on the next chapter), on which they are mounted. The hexapod, allows to control the tilts U, V, W and the parallel movements X, Y, Z along three orthogonal axis as can be seen in figure 13a and figure 13b. The simulations are essentially separated in two parts. The first part, is a scan through the focus for both IR and XUV beams for the optimal parameters, which is simply, a grazing angle of $5°$ for the incident beam, with the surface of the first toroidal mirror. The second part is a study of the aberration due to the misalignment of the beam with the system of the toroidal mirrors. The intensity of the beams is measured in units of the maximum intensity at the center of the beam at the starting surface. For, example if the beam has $100\,a.u.$ (arbitrary units) at the focus, It means that is 100 times the intensity at the center of the beam, at the starting surface. The focus of the XUV and IR beams that was calculated based on ray tracing is equal to $498.936\,mm$ measured from the center of the second toroidal mirror. The focus is the same for both of the beams, based on ray optics because the rays only reflect from the toroidal mirrors (reflection law doesn't depend on wavelength). In figure 13d can also be seen the the spot diagram through the focus of the beam. The elliptical shape of the rays' spots distribution is indicating that the beam is astigmatic around the focus.

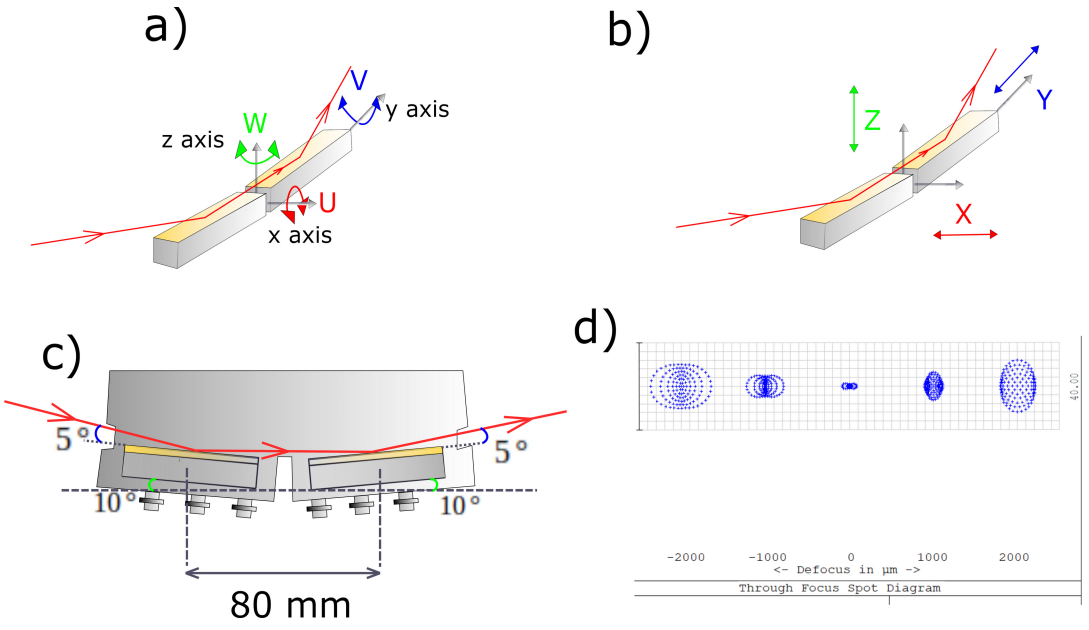

Figure 13: a) *W, Y, Z tilts of the system of toroidal mirrors, around x, y, z axis.* ***b)*** *Parallel movements X, Y, Z along x, y, z axis.* ***c)*** *Metal housing inside in which the toroidal mirrors are kept in order to be perfectly aligned and the angle and the distance between them be kept intact.* ***d)*** *Spot diagram through the focus of the beam. The oval shape of the rays' distribution reveals that the beams is astigmatic before, and after the focus.*

2.3.1 IR beam through the focus scan

In the figure 14a, is shown the images through the focus for an IR beam based on the parameters of section *2.2.1*. The full width on the images refers to the $2w(z)$ (beam diameter). The distance for each image is measured from the center of the second toroidal mirror. The analysis of the beam is done, by taking the line out along the two orthogonal x', y' axis, of a plane perpendicular to the beam direction. By fitting the data in figure 14b, the results of the simulations are shown in table 2. The maximum intensity is $I_{max(800\,nm)} = 1.9 \cdot 10^3 a.u.$.

Table 2: Results for the simulation of the IR beam (800 nm)

$D_{X'}(\mu m)$	$D_{Y'}(\mu m)$	$z_{RX'}(mm)$	$z_{RY'}(mm)$	$f_{X'}(mm)$	$f_{Y'}(mm)$
129.9 ± 0.4	130.98 ± 0.43	39.2 ± 1.5	42.4 ± 2.0	495.98 ± 0.31	495.4 ± 0.4

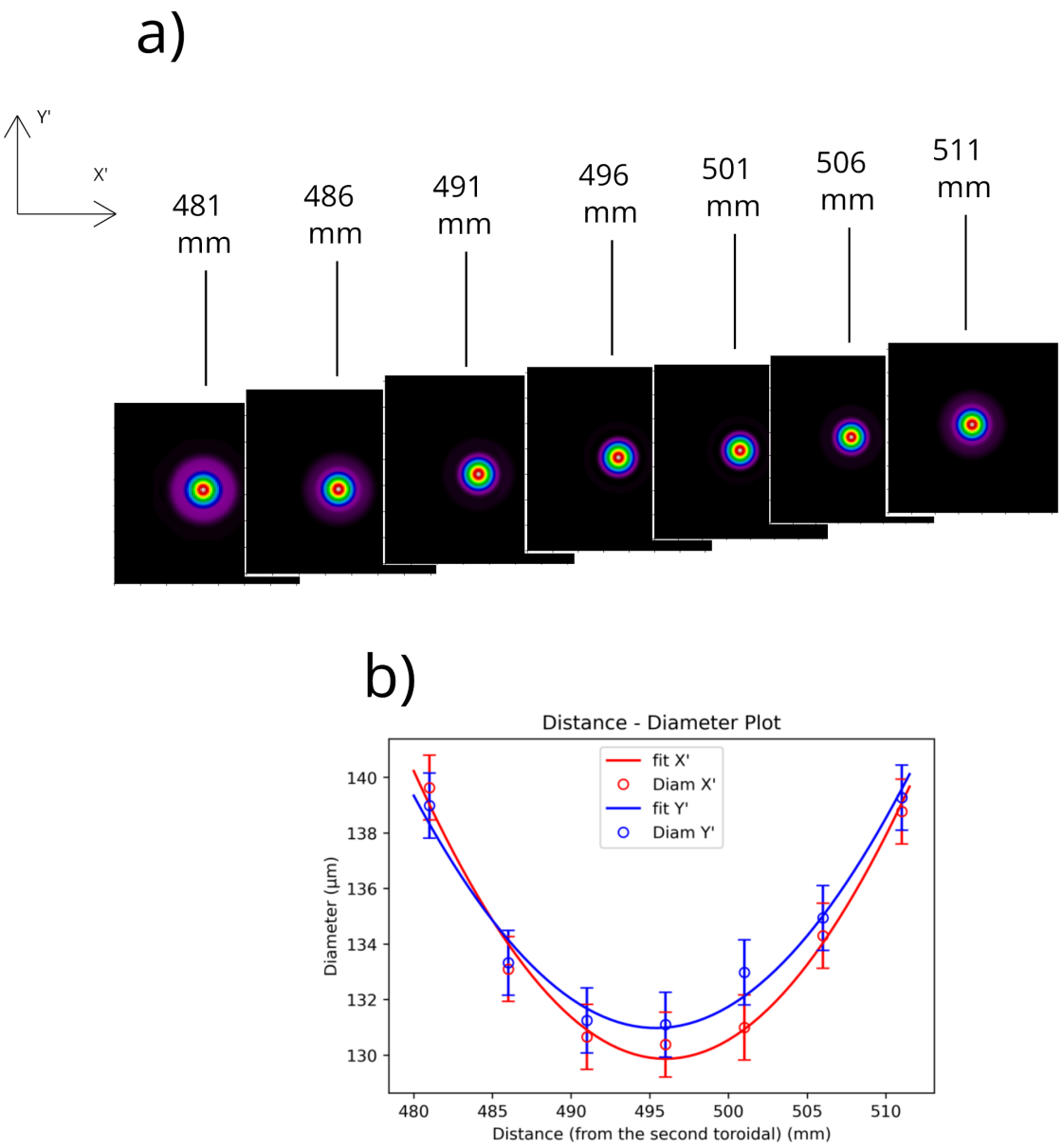

Figure 14: a) *Beam profiles of the IR beam (simulations), through the focus. The distances are measured from the second toroidal mirror.* ***b)*** *Plot of the beam diameter for x' and y' for different distances from the second toroidal mirror.*

2.3.2 XUV beam through the focus scan

The figure shows the profile of the XUV beam through the focus based on the parameters of section *2.2.1*. The calculations were done for the 13^{th} harmonic and the results of the simulations are shown in table 3. The results were acquired by fitting the data of figure 15b. The maximum intensity is $I_{max(61.54\,nm)} = 3.9 \cdot 10^5\, a.u.$.

Table 3: Results for the simulation of the XUV beam (61.54 nm)

$D_{X'}(\mu m)$	$D_{Y'}(\mu m)$	$z_{RX'}(mm)$	$z_{RY'}(mm)$	$f_{X'}(mm)$	$f_{Y'}(mm)$
9.38±0.40	9.44±0.22	1.97±0.24	2.13±0.16	499.4±0.1	498.7±0.1

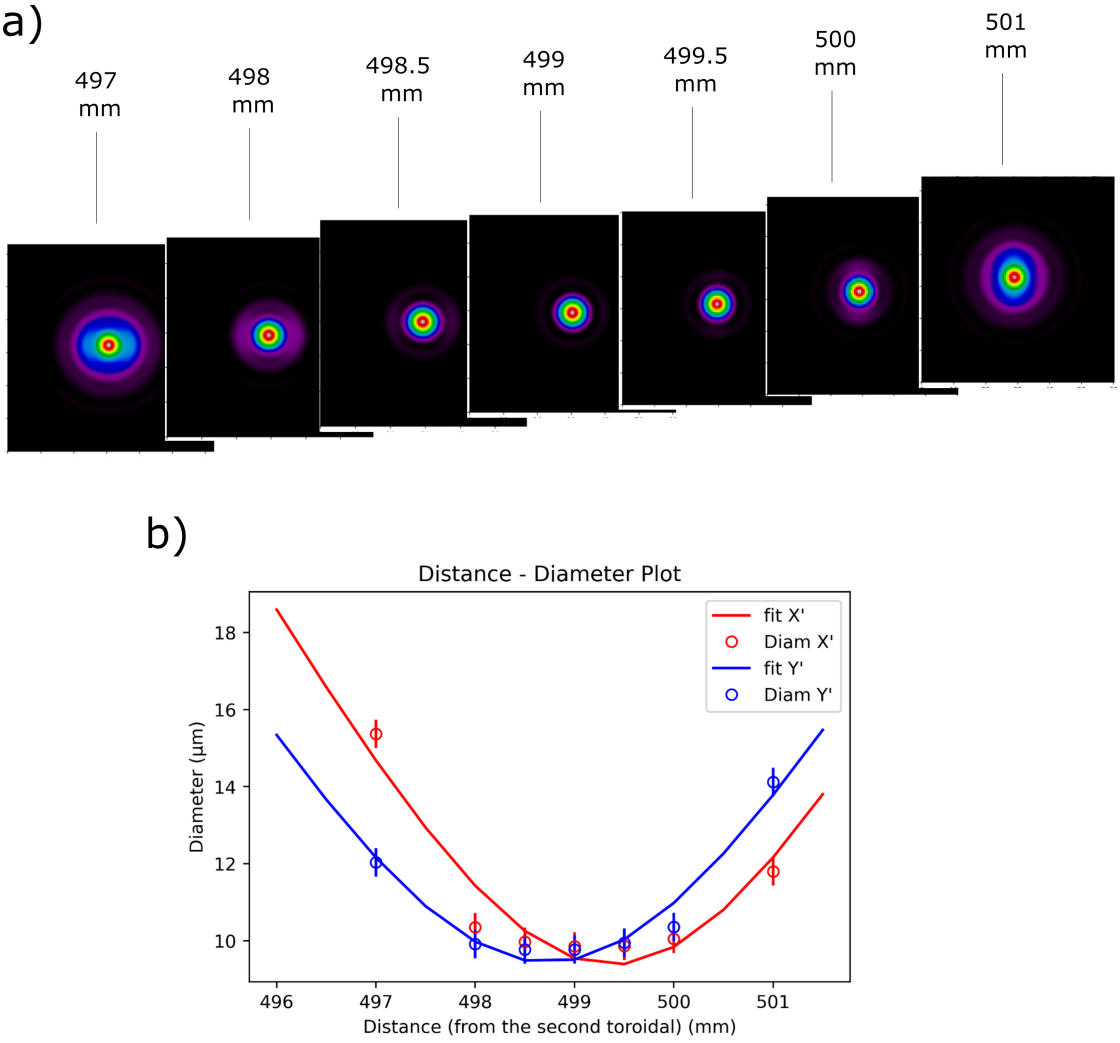

***Figure** 15: **a)** Beam profiles of the XUV beam (simulations) for the 13th, through the focus. The distances are measured from the second toroidal mirror. **b)** Plot of the beam diameter for x' and y' for different distances from the second toroidal mirror.*

The same calculations were done also for the the 25th harmonic. The beam profiles are shown in figure 16a and the results from the simulation are shown in table 4 (by fitting the data in figure 16b). The maximum intensity is $I_{max(32\,nm)}=1.3\cdot10^{6}\,a.u.$.

Table 4: Results for the simulation of the XUV beam (32 nm)

$D_{X'}(\mu m)$	$D_{Y'}(\mu m)$	$z_{RX'}(mm)$	$z_{RY'}(mm)$	$f_{X'}(mm)$	$f_{Y'}(mm)$
4.4 ± 0.8	3.9 ± 1.5	0.65 ± 0.17	0.53 ± 0.28	499.2 ± 0.1	498.8 ± 0.2

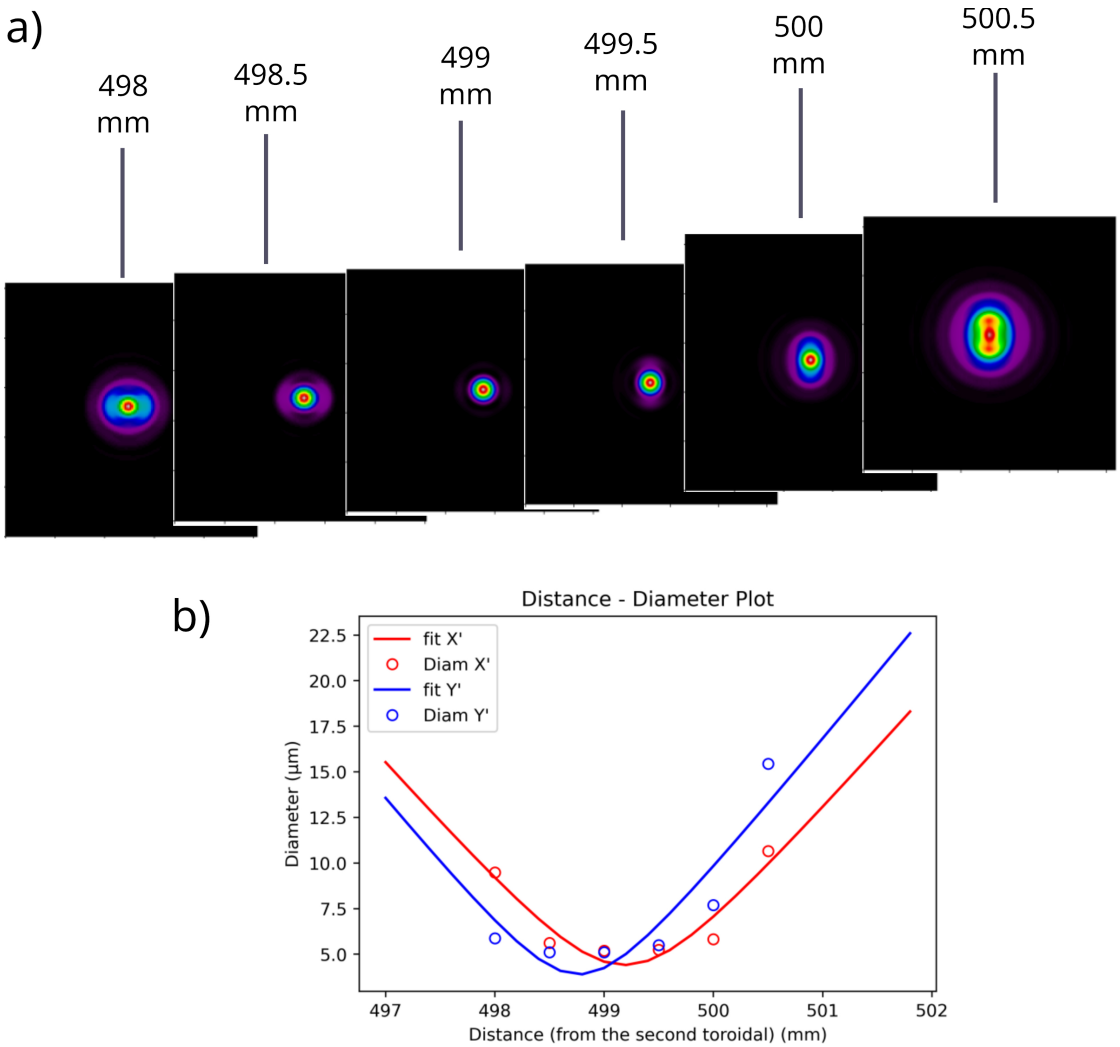

***Figure 16**: **a)** Beam profiles of the XUV beam (simulations) for the 13th, through the focus. The distances are measured from the second toroidal mirror. **b)** Plot of the beam diameter for x' and y' for different distances from the second toroidal mirror.*

2.3.3 Misalignment and aberrations for the IR beam

Based on the focus position that we calculated on *2.3.1* section for the IR beam, we now calculate the beam profile aberrations due to misalignment of the mirrors in relation with the beam. So, we change the tilts values, from their optimal values in order to see the effect on the beam profiles. Before proceeding with the results of the simulations, let's discuss some simple thoughts on the aberrations due to misalignment with the incoming beam. X and Y movements are not expected to insert additional aberrations to the system, because they only change the position where the beam strikes the surface of the mirrors. V tilt moves the whole focus position but does not change the shape of the beam. This is confirmed both experimentally (please see chapter 3) and from the simulations. So we will concentrate, only to the effect of the U, W tilts and Z movement. From the figures 17a, 17b, 17c, 17d, we observe that $\Delta U, \Delta W$ tilts change the beam profile to a star shape and add astigmatism. The figures 18c, 18d

show that ΔZ movement adds also astigmatism. There is no substantial drop in the intensity of the beam.

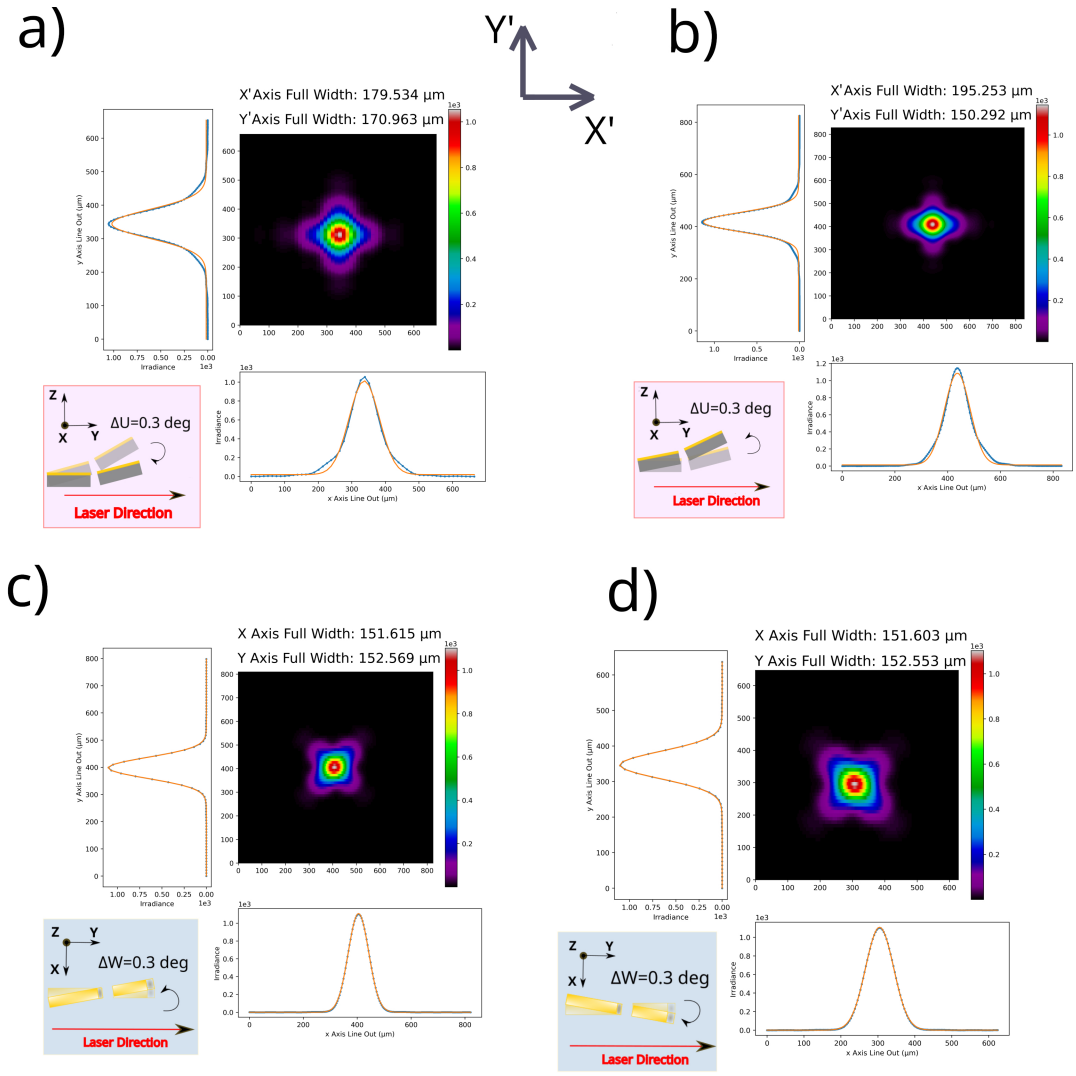

Figure 17: *Image of the IR beam on the focus for* ***a)*** *ΔU=-0.3 deg (deviation from the optimum value),* ***b)*** *ΔU=0.3 deg,* ***c)*** *ΔW=-0.3 deg,* ***d)*** *ΔW=0.3 deg.*

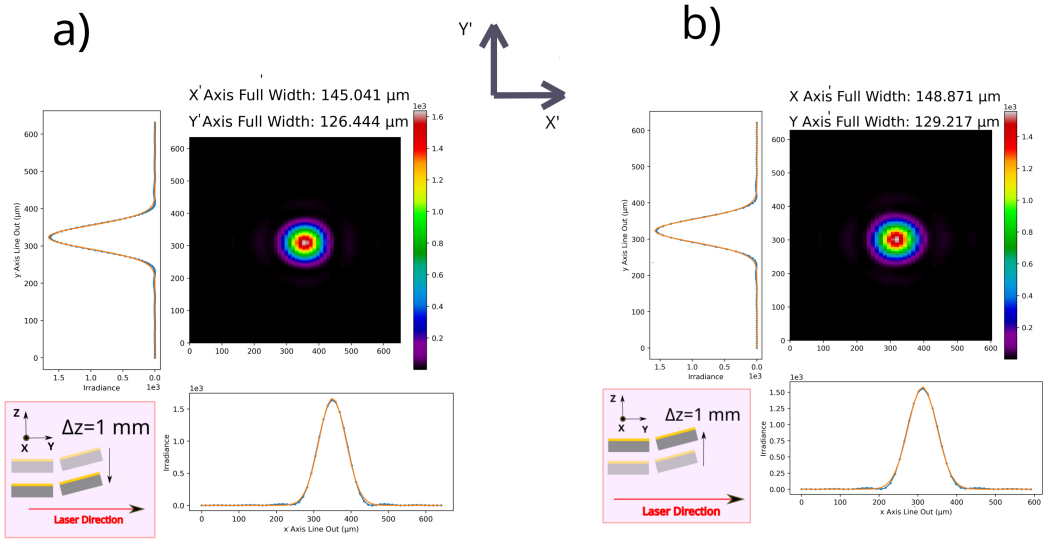

Figure 18: *Image of the IR beam on the focus for* ***a)*** *ΔZ=-1 mm (deviation from the optimum value),* ***b)*** *ΔZ=1 mm.*

2.3.4 Misalignment and aberrations for the XUV beams

Based on the focus position that we calculated on *2.3.2* section for the XUV beams (`13th and 25th harmonics), we now calculate the beam profile aberrations due to misalignment of the mirrors in relation with the beam. So once again, we change the tilts values, from their optimal values in order to see the effect on the beam profiles the results are shown in figures 19, 20.

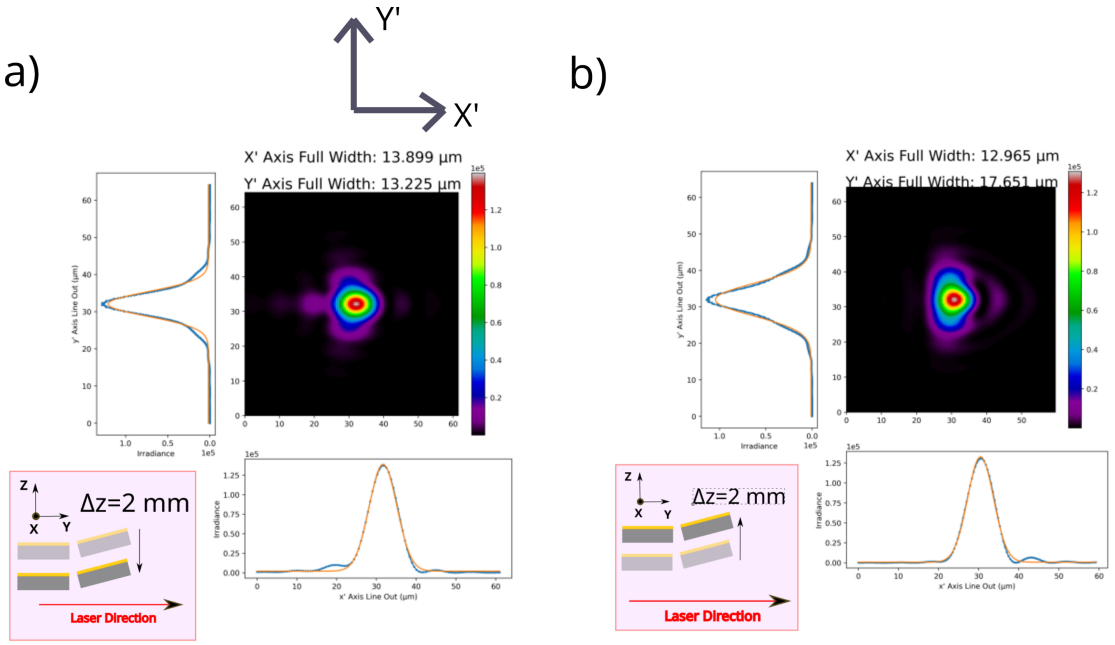

Figure 19*: Image of the XUV beam (13th harmonic) on the focus for* ***a)*** *ΔZ=-2 mm (deviation from the optimum value),* ***b)*** *ΔZ=2 mm.*

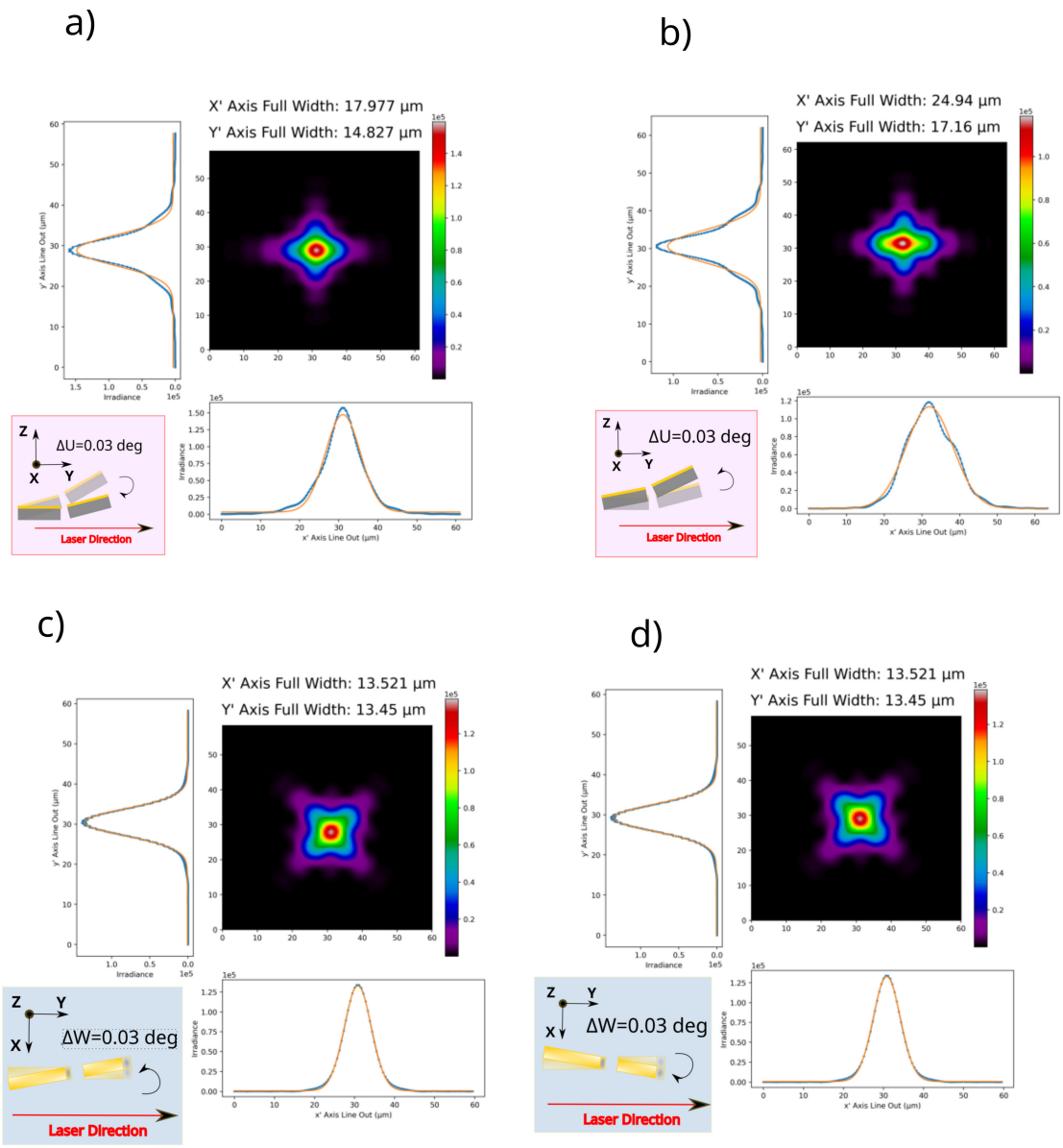

***Figure 20**: Image of the XUV beam (13th harmonic) on the focus for **a)** ΔU=-0.03 deg (deviation from the optimum value), **b)** ΔU=0.03 deg, **c)** ΔW=-0.03 deg, d) ΔW=-0.03 deg.*

The same calculations were repeated for the 25th harmonic, the beam profile aberrations due to misalignment of the mirrors is shown in figures 21, 22.

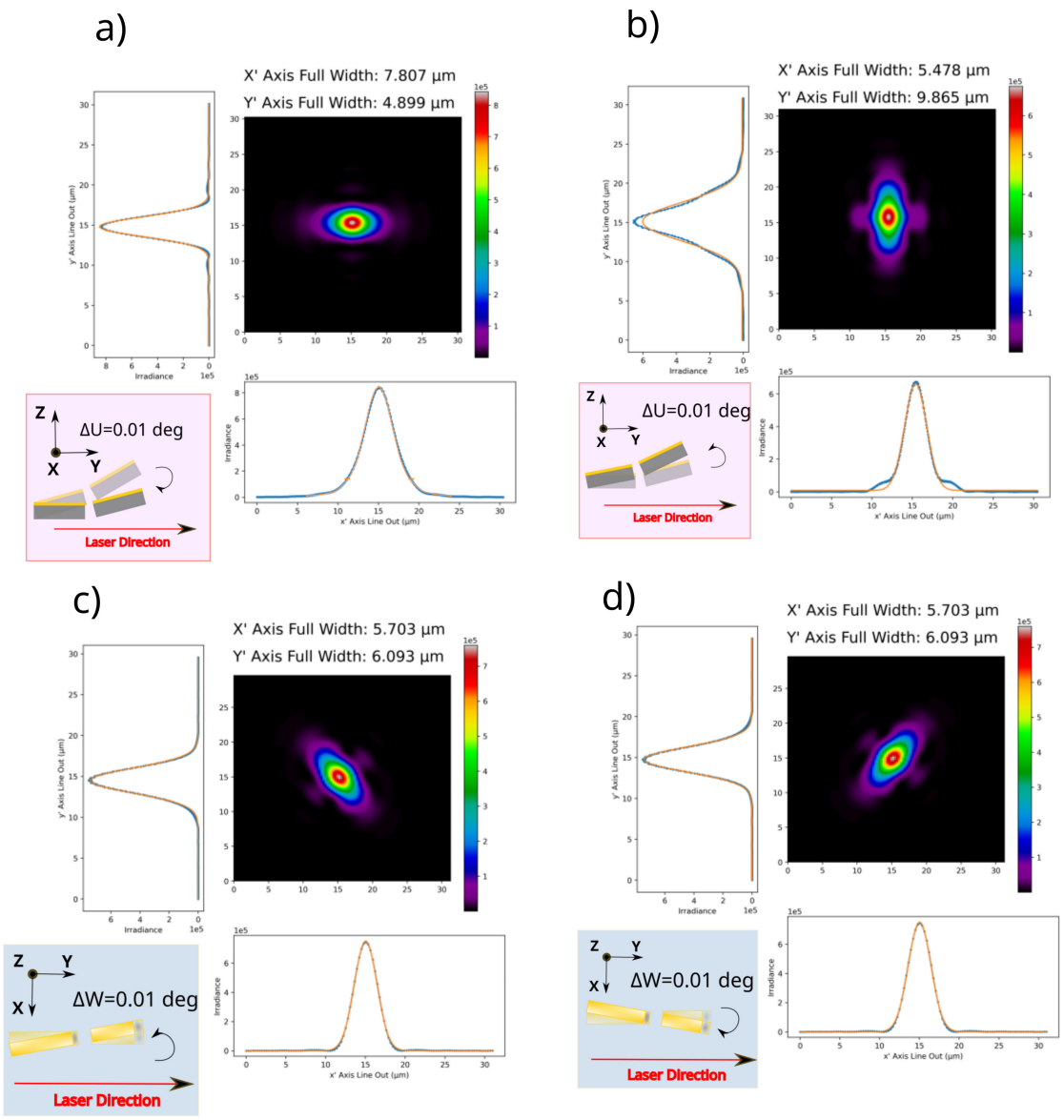

***Figure 21**: Image of the XUV beam (25th harmonic) on the focus for **a)** ΔU=-0.01 deg (deviation from the optimum value), **b)** ΔU=0.01 deg, **c)** ΔW=-0.01 deg, **d)** ΔW=0.01 deg.*

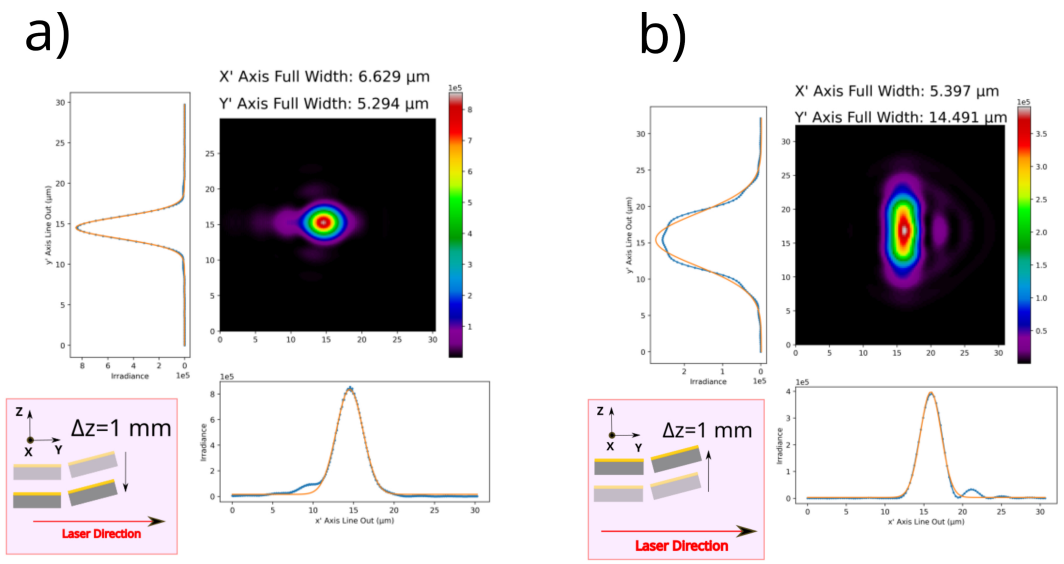

***Figure 22**: Image of the XUV beam (25th harmonic) on the focus for **a)** ΔZ=-1 mm (deviation from the optimum value), **b)** ΔZ=1 mm.*

From the results of figures 19, 20, 21, 22 we observe a similar behavior for the XUV beams (13th and 25th harmonics) as we did for the IR beam, regarding the beam aberrations due to deviation from the optimum values for the tilts of the toroidal mirrors. However, the XUV beams are 10 times more sensitive (13th harmonic), and 30 times more sensitive (25th harmonic), than the IR beam. This can easily be observed for example from the figures 17c, 17d (IR beam), 20c, 20d (13th harmonic), 21c, 21d (25th harmonic) where in order to observe the same effect on the beam profile (rotation and astigmatism) we have to make smaller rotations as the wavelength decreases, $0.3°$ (IR beam), $0.03°$ (13th harmonic), $0.01°$ (25th harmonic) respectively. The maximum drop Before ending this chapter, let's also make some quick calculations for the expected intensity at the focus of the XUV beam (25th harmonic). First we will assume that the power of the XUV pulse is $P_{ss}=0.1\,Gwatt$ and $w_{ss}=3.8\,mm$ at the starting surface of the simulation ($5000\,mm$ from the focus of the spherical mirror). The intensity at the center of the beam is then given at the focus of the beam after the pair of toroidal mirrors from the equation $I_{TorFocus}=I_{SS}\cdot I_{max(32nm)}=2P_{ss}/(\pi w_{ss}^{\,2})\cdot I_{max(32\,nm)}\Rightarrow$ $I_{TorFocus}\approx 5.7\cdot 10^{15}\,W/cm^2$ ($I_{max(32\,nm)}$ was calculated on section 2.3.2).

3 Experimental measurements and characterization of the focus of the IR beam

In this chapter we will describe the experimental procedure that we followed in order, to scan, find the focus of the IR beam and study experimentally the aberrations due to misalignment of the toroidal mirrors.

3.1 The experimental setup

In figure 23 can be seen the three last chambers of one of the branches of the Attosecond Science and Technology Laboratory at the Institute of Electronic Structure and Laser (IESL) which is part of the Foundation for Research and Technology Hellas (FORTH). The IR beam is steered from a silicon plate into the chamber with neutral density filters in order to attenuate the beam power. After that, the beam propagates to the chamber with the toroidal mirrors, which are mounted with the help of an aluminum custom made skeleton on a hexapod robot (PI H-824), which allows to make horizontal movements with a precision of $0.3\,\mu m$ along x, y, z axis (see figure 18), and also rotate around those axis with a precision of $3.5\,\mu rad$. The beam is focused from the pair of toroidal mirrors on the a CCD camera (WinCamD-UCD23) with a size $6.45\times 6.45\,\mu m$ per pixel. The CCD camera is mounted on custom x, y, z translation stage which is powered from two stepper motors on x, and z axis. The chambers are prepared and tested to be used under high vacuum conditions, with around $10^{-6}\sim 10^{-7}\,mbar$ pressure, for when the experiments with the XUV radiation will take place. The vacuum is prepared by using initially one scroll dry vacuum (Leybold SC 30D) with vacuum speed $30\,m^3/h$ in the CCD camera chamber and one dry vacuum pump (Pfeiffer CP 28) with vacuum speed $28\,m^3/h$. When the pressure reaches a value of around $0.01\,mbar$, 3 turbo vacuum pumps Pfeiffer HiPace 1200, 700, 300 start to operate inside the CCD camera, toroidal mirrors and ND filters chambers respectively. The average vacuum for the three turbo vacuum pumps are $260\,l/s$ (HiPace 300), $685\,l/s$ (HiPace 700) and $1300\,l/s$ (HiPace 1200).

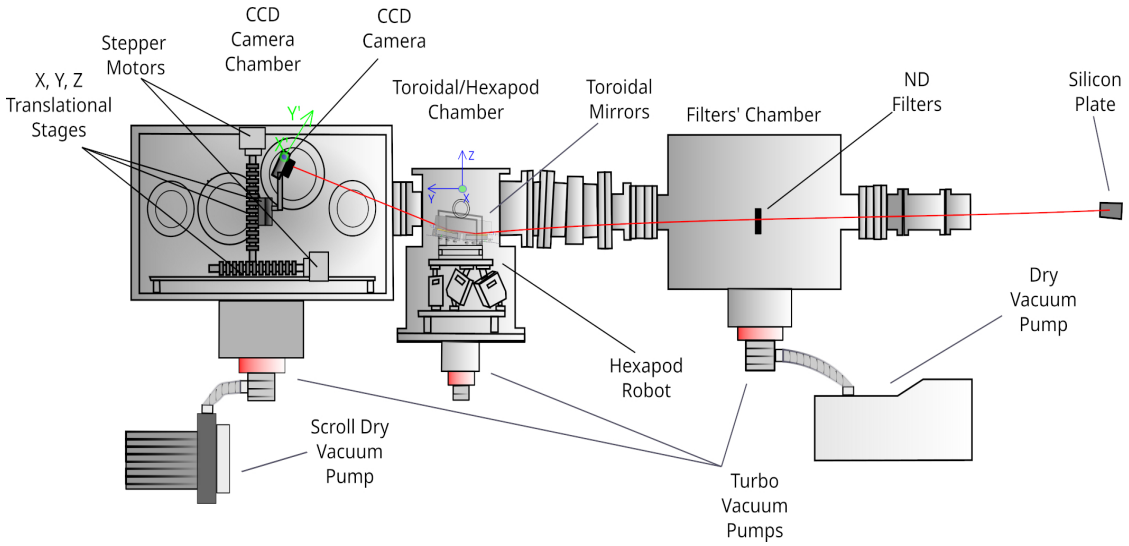

***Figure 23**: Experimental setup where the beam is reflected from the silicon plate, to neutral density filters and focused using a pair of toroidal mirrors, which their orientation is controlled from a hexapod robot device. The beam profile is recorded from a CCD which can be moved along the axis of beam propagation. X'Y' is the orthogonal axis on the surface of the CCD camera and XYZ are the axis on the chamber of hexapod robot.*

3.2 Experimental beam profiles around the IR beam's focus

In this section is shown the results from beam profile images through the focus, after the reflection from the pair of toroidal mirrors. The images are taken along the beam's propagation axis, with a CCD camera that can move with a precision of $0.5\,mm$ in $3D$ space. The line outs of the beam profile, are take along X',Y' axis (please see figure 23). The distances, are measured from the center of the second toroidal mirror. The range of measured signal for each pixel is $0\sim65000\,a.u.$. By a trial and error method, and real time observation of the beam profile, we chosen a set of values for X,Y,Z position and U,W,V tilts which where kept unchanged during the acquisition of beam profile around the focus. The criterion for the choice of the parameters for the orientation of the hexapod, was chosen based on a good beam quality (spot size and shape) near the focus region. The measurements for the beam profiles are shown in figure 24a, and the results for the beam parameters (acquired from fitting the data in figure 24b) are shown in table 5. Based on the results of table 5, the differences in $f_{x'}$ and $f_{y'}$ mean that the focus exhibits a rather small astigmatism and the system is not fully optimized (most probably the angle of incidence is not exactly 5°).

Table 5: Results for the experimental measurements of the IR beam (800 nm)

$D_{X'}(\mu m)$	$D_{Y'}(\mu m)$	$z_{RX'}(mm)$	$z_{RY'}(mm)$	$f_{X'}(mm)$	$f_{Y'}(mm)$
177.3 ± 5.6	146.9 ± 2.8	40.4 ± 3.6	28.31 ± 0.98	508.1 ± 1.9	496.8 ± 0.7

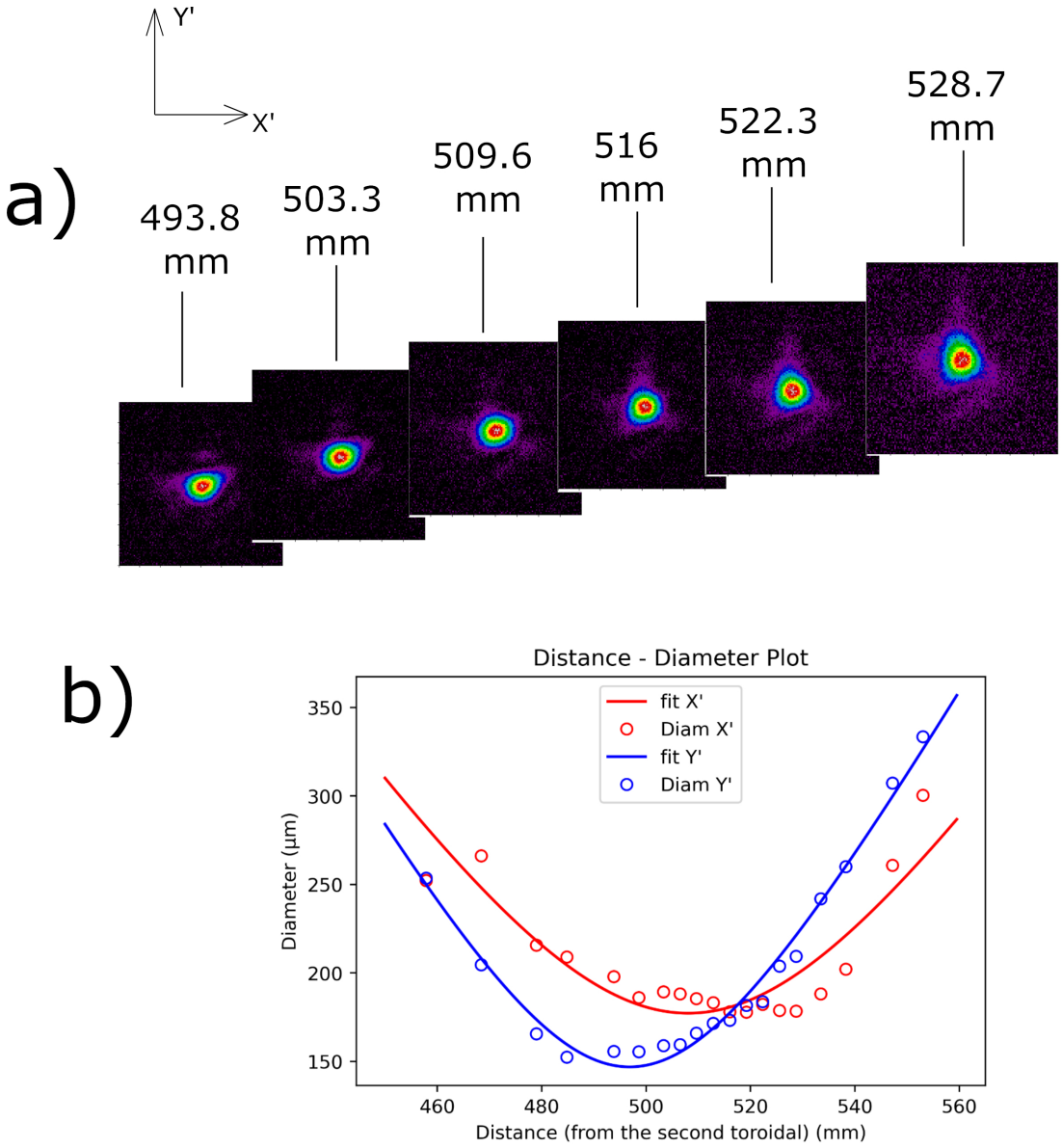

***Figure 24**: **a)** Beam profiles of the IR beam (simulations), through the focus. The distances are measured from the second toroidal mirror. **b)** Plot of the beam diameter for x' and y' for different distances from the second toroidal mirror.*

3.3 Experimental study of aberrations due to misalignment of the toroidal mirrors

Based on the images of figure 24a and with the criterion of minimizing the ellipticity of the beam, the CCD camera was placed on a position with a distance of around $516\,mm$ from the second toroidal mirror (please see the central beam profile of figure 24a), as the point to study the aberrations due to misalignment of the toroidal mirrors with the incident beam. The beam diameters are $D_X = 178.182\,\mu m$ and $D_Y = 173.268\,\mu m$, and with $e = D_Y / D_X \approx 0.97$ (ellipticity). Based on the experimental parameters chosen for the X, Y, Z positions and the tilts of the toroidal mirrors (their orientation is determined, from the movement of the hexapod), we will study how the beam profile is affected on the focused spot when small changes are induced on the toroidal mirrors orientation. The results are shown on figures 25, 26, 27. Each image contains information about the beam profile, the movement of the toroidal mirrors and the displacement of the beam in $3D$ space compared to the starting position.

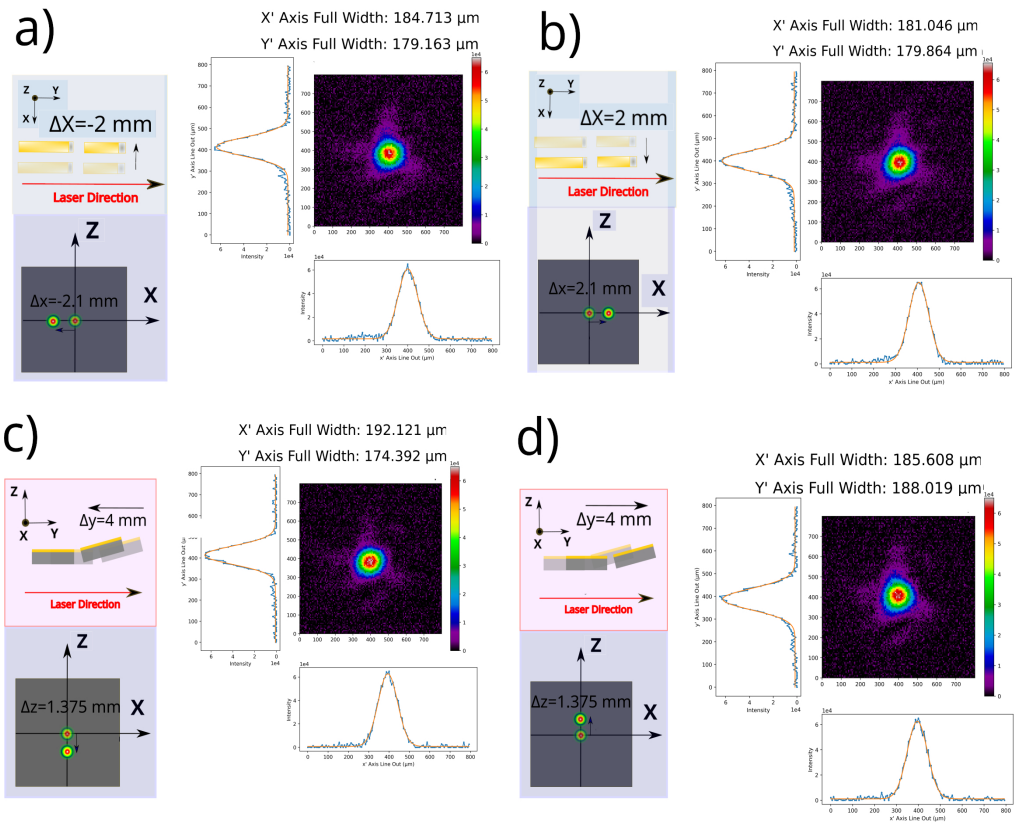

***Figure 25**: Beam profile and movement of the beam's position in 3D space for a small displacement **a)** ΔX=-2 mm, **b)** ΔX=2 mm, **c)** ΔY=-4 mm, **d)** ΔY=4 mm. For each image is also shown, the displacement of the toroidal mirrors, compared to their starting position.*

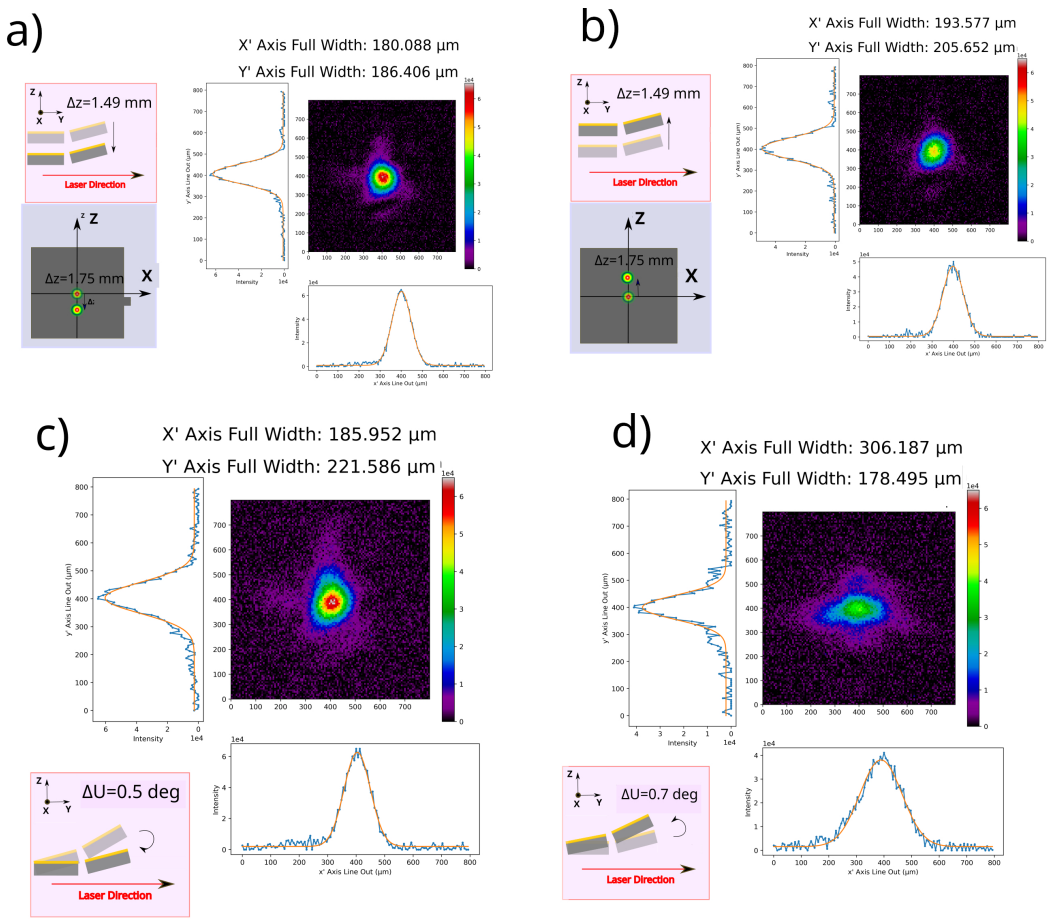

***Figure 26**: Beam profile and movement of the beam's position in 3D space for a small displacement (or a small rotation) **a)** Δz=-1.49mm, **b)** Δz=1.49 mm, **c)** ΔU=-0.5 deg, **d)** ΔU=0.7 deg. For each image is also shown, the displacement of the toroidal mirrors, compared to their starting position.*

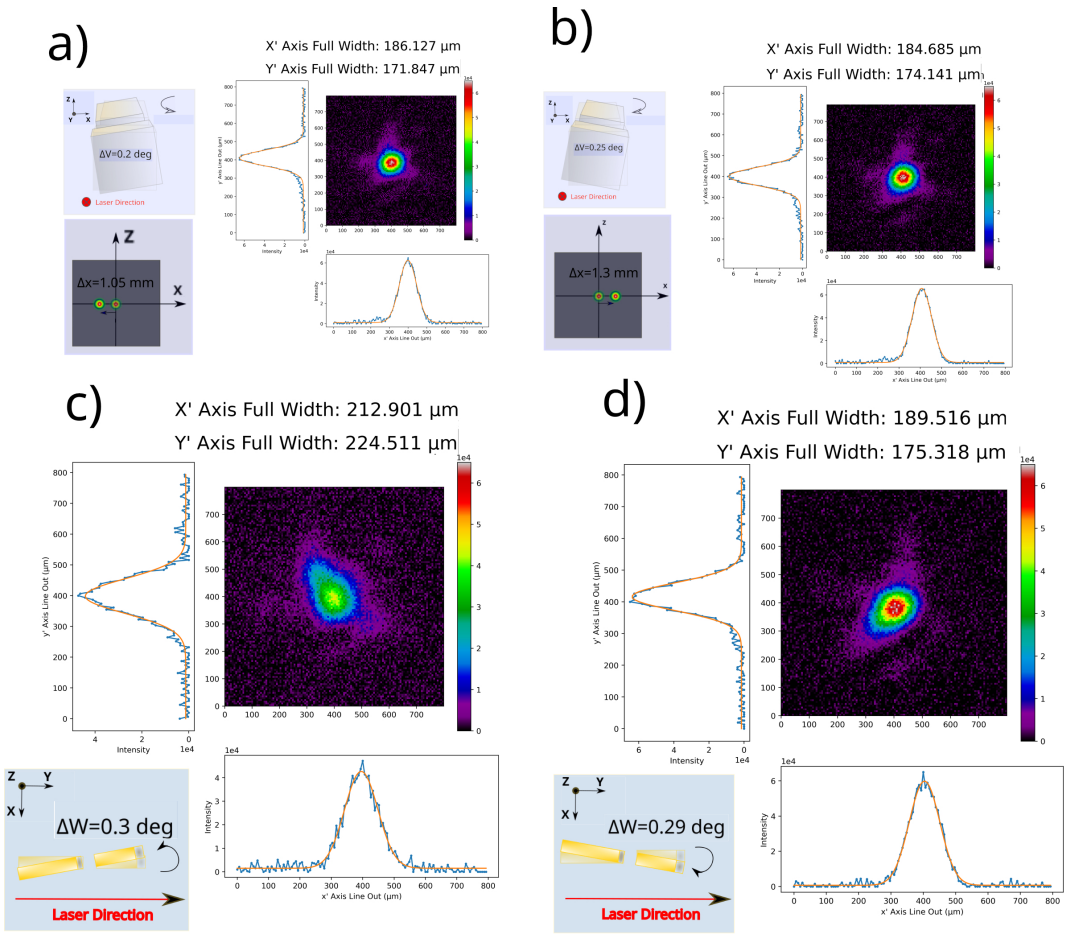

***Figure 27**: Beam profile and movement of the beam's position in 3D space for a small displacement (or a small rotation) **a)** ΔV=-0.2 deg, **b)** ΔV=0.25 deg, **c)** ΔW=-0.3 deg, **d)** ΔW=0.29 deg. For each image is also shown, the displacement of the toroidal mirrors, compared to their starting position.*

3.3.1 Analysis of the experimental results and comparison with the computational data

From the images of the group of small displacements of X, Y, Z we observe that ΔX displacement (figures 25a, 25b), increases the beam diameter for both axis (~3.4% increase), and moves the beam along x axis (~2 mm movement). ΔY movement (figures 25c, 25d) changes the beam diameter (~7.9 % increase), for each axis and It also moves the beam along y axis (~1.4 mm movement). The ΔZ movement increases the beam diameter (~1.1 % increase), and also reduces the beams intensity as a smaller part of the beam strikes the first mirror, due to the physical aperture of the metallic housing of the toroidal mirrors. (figures 26a, 26b). ΔZ displacement, also moves the beam along y axis (~1.8 mm movement). For the group of rotations ΔU tilt (figures 26c, 26d), inserts astigmatism (~71% beam diameter increase), changes the ellipticity ($e \approx 0.58$) of the beam and reduces the intensity due to the change of the angle of incidence (also changes the reflectivity). ΔV rotation (figures 27a, 27b) does not affect the beam profile, but moves the beam along x axis (~1.3 mm movement), which was expected, as It redirects the rays due to the rotation. Finally ΔW tilt also reduces the intensity because the metallic case aperture blocks part of the beam and rotates the beam around the center of x', y' axis (~ $30°$ rotation). There is also an increase of the beam diameter (~19% increase).

Compared to the simulation, Zemax predicted accurately that X, Y, V movements do not really change the beam profile which can be concluded by a simple ray trace. It also predicted the rotation of beam due to ΔW (figures 17c, 17d) and the astigmatism due to the ΔZ (figures 18a, 18b). However, a drop on the intensity of the beam was not predicted which can be explained from the fact that, the setup of the simulation, is not exactly the same as the experimental setup inside the laboratory (difference in physical apertures etc.). The computational model, predicted a rayleigh range of around $z_{Rx'(simu)} \approx 39.2 \pm 1.5\, mm$ which is close to the experimental rayleigh range value $z_{Rx'(\exp)} \approx 40.4 \pm 3.6\, mm$ for x' axis. The difference in rayleigh range value for $z_{Ry'(simu)} \approx 42.4 \pm 2.0\, mm$ compared to $z_{Ry'(\exp)} \approx 28.31 \pm 0.98\, mm$, is due to the astigmatism of the beam and maybe a difference in divergence, and the beam size of the beam of the simulation compared to the beam of the experiment. The same arguments can also explain the difference between the $2w_{0x'(simu)} \approx 129.9 \pm 0.4\, \mu m$, $2w_{0y'(simu)} \approx 130.98 \pm 0.43\, \mu m$ of the simulations compared to the values $2w_{0x'(\exp)} \approx 177.3 \pm 5.6\, \mu m$, $2w_{0y'(\exp)} \approx 146.9 \pm 2.8\, \mu m$ from the experimental data. The beam of the simulations, did not suffer from astigmatism close to the focus region ($f_{x'(simu)} = 495.98 \pm 0.31\, mm$, $f_{y'(simu)} = 495.4 \pm 0.4\, mm$), compared to the microfocused experimental beam which suffered from astigmatism ($f_{x'(\exp)} = 508.1 \pm 1.9$, $f_{y'(\exp)} = 496.8 \pm 0.7\, mm$) with a difference of around $11\, mm$ for the x', y' foci.

4 Conclusion

During the process of this thesis, we managed to make a computational model based on the experimental setup, of a pair of toroidal mirrors mounted on hexapod robot device and characterize the system through gathering and analyzing experimental data. Important parameters of the setup where calculated, both experimentally and computationally (focal length, rayleigh range, beam, reflectivity of the system) for the IR beam and the same parameters were calculated for the XUV beams (13^{th} and 25^{th} harmonics) via simulations with Zemax. The characterization of the system, was done via measuring the beam profile around the focus region and further studying the effects of toroidal mirrors' misalignment on the beam profile, for a position very close to the focus. This is the first step, towards the optimization of the setup parameters (hexapod position), in order to minimize the astigmatism and achieve a exceptional focusing conditions for the IR beam. Finding those condition, will eventually lead to achieving optimum focusing conditions also for the XUV beam. The setup is intended to be used, for pump probe experiments with a broad range of high XUV photon energies.

5 Bibliography

[1] Hentschel, M., Kienberger, R., Spielmann, C., Reider, G. A., Milosevic, N., Brabec, T., Corkum, P., Heinzmann, U., Drescher, M., & Krausz, F. (2001). Attosecond metrology. *Nature*, *414*(6863), 509–513. https://doi.org/10.1038/35107000.

[2] Paul, P. M. (2001). Observation of a Train of Attosecond Pulses from High Harmonic Generation. *Science*, *292*(5522), 1689–1692. https://doi.org/10.1126/science.1059413.

[3] Drescher, L., Kornilov, O., Witting, T., Reitsma, G., Monserud, N., Rouzée, A., Mikosch, J., Vrakking, M. J. J., & Schütte, B. (2018). Extreme-ultraviolet refractive optics. *Nature*, *564*(7734), 91–94. https://doi.org/10.1038/s41586-018-0737-3.

[4] Schnürer, M., Cheng, Z., Hentschel, M., Krausz, F., Wilhein, T., Hambach, D., Schmahl, G., Drescher, M., Lim, Y., & Heinzmann, U. (2000). Few-cycle-driven XUV laser harmonics: generation and focusing. *Applied Physics B*, *70*(S1), S227–S232. https://doi.org/10.1007/s003400000286.

[5] Coudert-Alteirac, H., Dacasa, H., Campi, F., Kueny, E., Farkas, B., Brunner, F., Maclot, S., Manschwetus, B., Wikmark, H., Lahl, J., Rading, L., Peschel, J., Major, B., Varjú, K., Dovillaire, G., Zeitoun, P., Johnsson, P., L'Huillier, A., & Rudawski, P. (2017). Micro-Focusing of Broadband High-Order Harmonic Radiation by a Double Toroidal Mirror. *Applied Sciences*, *7*(11), 1159. https://doi.org/10.3390/app7111159.

[6] Wieland, M., Wilhein, T., Spielmann, C., & Kleineberg, U. (2003). Zone-plate interferometry at 13 nm wavelength. *Applied Physics B*, *76*(8), 885–889. https://doi.org/10.1007/s00340-003-1233-4.

[7] Cao, Q., & Jahns, J. (2004). Comprehensive focusing analysis of various Fresnel zone plates. *Journal of the Optical Society of America A*, *21*(4), 561. https://doi.org/10.1364/josaa.21.000561.

[8] Le Déroff, L., Salières, P., & Carré, B. (1998). Beam-quality measurement of a focused high-order harmonic beam. *Optics Letters*, *23*(19), 1544. https://doi.org/10.1364/ol.23.001544.

[9] Tzallas, P., Witte, K., Tsakiris, G., Papadogiannis, N., & Charalambidis, D. (2004). Extending optical fs metrology to XUV attosecond pulses. *Applied Physics A*, *79*(7), 1673–1677. https://doi.org/10.1007/s00339-004-2680-4.

[10] Poletto, L., Frassetto, F., Calegari, F., Anumula, S., Trabattoni, A., & Nisoli, M. (2013). Micro-focusing of attosecond pulses by grazing-incidence toroidal mirrors. *Optics Express*, *21*(11), 13040. https://doi.org/10.1364/oe.21.013040.

[11] Attwood, D. (1999). *Soft X-Rays and Extreme Ultraviolet Radiation: Principles and Applications*. Cambridge University Press.

[12] *Optical materials*. (n.d.-b). Newport. Retrieved June 26, 2021, from https://www.newport.com/n/optical-materials.

[13] *X-Ray Interactions With Matter*. (n.d.). CXRO. Retrieved June 26, 2021, from https://henke.lbl.gov/optical_constants/.

[14] Rolt, S. (2020). *Optical Engineering Science* (1st ed.). Wiley.

[15] Bourassin-Bouchet, C., Mang, M. M., Delmotte, F., Chavel, P., & de Rossi, S. (2013). How to focus an attosecond pulse. *Optics Express*, *21*(2), 2506. https://doi.org/10.1364/oe.21.002506.

[16] Tsatrafyllis, N., Bergues, B., Schröder, H., Veisz, L., Skantzakis, E., Gray, D., Bodi, B., Kuhn, S., Tsakiris, G. D., Charalambidis, D., & Tzallas, P. (2016). The ion microscope as a tool for quantitative measurements in the extreme ultraviolet. *Scientific Reports*, *6*(1). https://doi.org/10.1038/srep21556.

[17] Gautier, J., Delmotte, F., Roulliay, M., Bridou, F., Ravet, M. F., & Jérome, A. (2005). Study of normal incidence of three-component multilayer mirrors in the range 20–40 nm. *Applied Optics*, *44*(3), 384. https://doi.org/10.1364/ao.44.000384.

[18] Morlens, A. S., López-Martens, R., Boyko, O., Zeitoun, P., Balcou, P., Varjú, K., Gustafsson, E., Remetter, T., L'Huillier, A., Kazamias, S., Gautier, J., Delmotte, F., & Ravet, M. F. (2006b). Design and characterization of extreme-ultraviolet broadband mirrors for attosecond science. *Optics Letters*, *31*(10), 1558. https://doi.org/10.1364/ol.31.001558.

[19] Yakubovsky, D. I., Arsenin, A. V., Stebunov, Y. V., Fedyanin, D. Y., & Volkov, V. S. (2017). Optical constants and structural properties of thin gold films. *Optics Express*, *25*(21), 25574. https://doi.org/10.1364/oe.25.025574.

[20] Wolter, H. (1952). Spiegelsysteme streifenden Einfalls als abbildende Optiken für Röntgenstrahlen. *Annalen Der Physik*, *445*(1–2), 94–114. https://doi.org/10.1002/andp.19524450108.

[21] Trümper, J. E., & Hasinger, G. (2016). *The Universe in X-Rays (Astronomy and Astrophysics Library)* (Softcover reprint of the original 1st ed. 2008 ed.). Springer.

[22] *Curved mirror optics*. (n.d.). X-Ray Optics. Retrieved June 26, 2021, from http://www.x-ray-optics.de/index.php/en/types-of-optics/reflecting-optics/curved-mirrors.

[23] Ornigotti, M., & Aiello, A. (2014). Analytical Approximations of Whispering Gallery Modes in Anisotropic Ellipsoidal Resonators. *Physics Research International*, *2014*, 1–10. https://doi.org/10.1155/2014/615605.

[24] Makos, I., Orfanos, I., Nayak, A., Peschel, J., Major, B., Liontos, I., Skantzakis, E., Papadakis, N., Kalpouzos, C., Dumergue, M., Kühn, S., Varju, K., Johnsson, P., L'Huillier, A., Tzallas, P., & Charalambidis, D. (2020). A 10-gigawatt attosecond source for non-linear XUV optics and XUV-pump-XUV-probe studies. *Scientific Reports*, *10*(1). https://doi.org/10.1038/s41598-020-60331-9.

[25] *Physical Measurement Laboratory*. (2021, June 29). NIST. https://www.nist.gov/pml

[26] Zemax LLC. (2014). *Zemax 13 Optical Design Program: User's Manual*.

[27] B.E.A., S. (2021). *Fundamentals Of Photonics, 2nd Edition*. Wiley India.

[28] Born, M., & Wolf, E. (2020). *Principles of Optics: 60th Anniversary Edition* (7th ed.). Cambridge University Press.

[29] Shannon, R. R., & Wyant, J. C. *Applied Optics and Optical Engineering* (Vol. 11). Academic Press.

[30] Joseph W. Goodman. (2017). Introduction to Fourier Optics (4th ed.). W. H. Freeman.

[31] Chatziathanasiou, S., Kahaly, S., Charalambidis, D., Tzallas, P., & Skantzakis, E. (2019). Imaging the source of high-harmonics generated in atomic gas media. *Optics Express*, *27*(7), 9733. https://doi.org/10.1364/oe.27.009733.

[32] Quintard, L., Strelkov, V., Vabek, J., Hort, O., Dubrouil, A., Descamps, D., Burgy, F., Péjot, C., Mével, E., Catoire, F., & Constant, E. (2019). Optics-less focusing of XUV high-order harmonics. *Science Advances*, *5*(4), eaau7175. https://doi.org/10.1126/sciadv.aau7175